

ORIGINAL RESEARCH ARTICLE

Methane seepage in a Cretaceous greenhouse world recorded by an unusual carbonate deposit from the Tarfaya Basin, Morocco

DANIEL SMRZKA*, JENNIFER ZWICKER*, SADAT KOLONIC†, DANIEL BIRGEL‡, CRISPIN T.S. LITTLE§, AKMAL M. MARZOUK¶, EL HASSANE CHELLAI**, THOMAS WAGNER†† and JÖRN PECKMANN*,‡ ID

*Department für Geodynamik und Sedimentologie, Universität Wien, 1090 Wien, Austria

†Shell Petroleum Development Company of Nigeria, Port Harcourt, Nigeria

‡Institut für Geologie, Universität Hamburg, Bundesstraße 55, 20146 Hamburg, Germany (E-mail: joern.peckmann@uni-hamburg.de)

§School of Earth and Environment, University of Leeds, Leeds, LS2 9JT, UK

¶Geology Department, Faculty of Science, Tanta University, 31527 Tanta, Egypt

**Department of Geology, Faculty of Sciences Semlalia, Cadi Ayyad University, Marrakech, Morocco

††Lyell Centre, Heriot-Watt University, Edinburgh, EH14 4AS, UK

Keywords

Black shales, carbonate authigenesis, cold seeps, oceanic anoxic events, Tarfaya Basin.

Manuscript received: 30 November 2016;

Accepted: 8 February 2017

The Depositional Record 2017; 3(1): 4–37

doi: 10.1002/dep2.24

ABSTRACT

During the Cretaceous major episodes of oceanic anoxic conditions triggered large scale deposition of marine black shales rich in organic carbon. Several oceanic anoxic events (OAEs) have been documented including the Cenomanian to Turonian OAE 2, which is among the best studied examples to date. This study reports on a large limestone body that occurs within a black shale succession exposed in a coastal section of the Tarfaya Basin, Morocco. The black shales were deposited in the aftermath of OAE 2 in a shallow continental sea. To decipher the mode and causes of carbonate formation in black shales, a combination of element geochemistry, palaeontology, thin section petrography, carbon and oxygen stable isotope geochemistry and lipid biomarkers are used. The ^{13}C -depleted biphytanic diacids reveal that the carbonate deposit resulted, at least in part, from microbially mediated anaerobic oxidation of methane in the shallow subseafloor at a hydrocarbon seep. The lowest obtained $\delta^{13}\text{C}_{\text{carbonate}}$ values of -23.5‰ are not low enough to exclude other carbon sources than methane apart from admixed marine carbonate, indicating a potential contribution from *in situ* remineralization of organic matter contained in the black shales. Nannofossil and trace metal inventories of the black shales and the macrofaunal assemblage of the carbonate body reveal that environmental conditions became less reducing during the deposition of the background shales that enclose the carbonate body, but the palaeoenvironment was overall mostly characterized by high productivity and episodically euxinic bottom waters. This study reconstructs the evolution of a hydrocarbon seep that was situated within a shallow continental sea in the aftermath of OAE 2, and sheds light on how these environmental factors influenced carbonate formation and the ecology at the seep site.

INTRODUCTION

The Cretaceous was a period in Earth history when major episodes of oceanic anoxic conditions led to large scale accumulation of organic matter in marine sediments (Arthur & Sageman, 1994; Larson & Erba, 1999; Jones & Jenkyns, 2001). These organic-rich deposits have been

termed black shales, and phases of their coeval and repeated occurrence in the Phanerozoic rock record have been referred to as oceanic anoxic events (OAEs, Schlanger & Jenkyns, 1976; Weissert *et al.*, 1979; Schlanger *et al.*, 1987; Kerr, 1998; Jenkyns, 2003; Meyer & Kump, 2008). Sea-level was markedly elevated during some periods of the Cretaceous compared to the present due to the

warm, equable climate (Sames *et al.*, 2016 and references therein). The expansion of shallow epicontinental seas, where upwelling and enhanced nutrient flux from the continents increased primary production, enabled the accumulation of organic carbon-rich sediments in water depths of several hundreds of metres (Hallam & Bradshaw, 1977; Weissert, 1981; Kuhnt *et al.*, 1990; Arthur & Sageman, 1994). Two processes held primarily responsible for the deposition of black shales are (1) pulses of enhanced primary productivity accompanied by elevated atmospheric carbon dioxide concentrations and sea surface temperatures (Barron, 1983; Ingall *et al.*, 1993; Forster *et al.*, 2007), and (2) the increased preservation of organic matter within restricted, stratified, oxygen-deficient basins (Masle *et al.*, 1997; Meyer & Kump, 2008). With supporting evidence for both scenarios, it is likely that both production and preservation in stratified basins increased sequestration rates of organic carbon in Cretaceous marine sediments (Jenkyns *et al.*, 2007; Owens *et al.*, 2013).

Several OAEs have been documented during the Cretaceous including the Aptian to Albian OAE 1, the Cenomanian to Turonian OAE 2 and the Coniacian to Santonian OAE 3 (Jenkyns, 2010 and references therein). The OAE 2, or Bonarelli event (Bonarelli, 1891; Schlanger *et al.*, 1987), is among the best studied examples to date. High rates of sea floor spreading and volcanic activity – both linked to the breakup of Gondwana with the formation of early ocean basins as carbon sinks and the evolution of ocean gateways – led to increasing atmospheric carbon dioxide concentrations followed by a significant turnover of ocean chemistry and extinctions of marine biota (Brumsack, 1980; Arthur *et al.*, 1985; Larson, 1991; Kaiho, 1994; Wagner & Pletsch, 1999; Gale *et al.*, 2000; McAnena *et al.*, 2013). Black shales related to OAE 2 have been reported from many parts of the world including the proto southern North Atlantic and eastern Tethys Oceans (Lüning *et al.*, 2004). During OAE 2 the Tethys and Atlantic Oceans were affected by sluggish circulation of bottom waters caused by the shallow and partly closed connections to neighbouring oceans (Kuypers *et al.*, 2002). Replenishment of oxygen was impeded within these partially isolated basins, favouring the development of anoxic and, possibly, euxinic conditions even in the photic zone (Herbin *et al.*, 1986; Baudin, 1995; Sinninghe Damsté & Köster, 1998; Handoh *et al.*, 1999). Large areas of the continental shelf and slope along the northern parts of Algeria, Libya, Tunisia and Morocco were deprived of oxygen, and enabled the rapid accumulation of shales and limestones rich in organic carbon linked to cyclic perturbations of redox-nutrient cycles and orbital forcing (Leine, 1986; El Albani *et al.*, 1999a; Nederbragt & Fiorentino, 1999; Kolonic *et al.*, 2005; Poulton *et al.*,

2015; for Atlantic-wide teleconnections see Wagner *et al.*, 2013 and references therein).

The Cretaceous has yielded several unusual carbonate deposits occurring before, during and after the OAEs. Some of these deposits have been ascribed to carbonate precipitation related to chemosynthesis-based microbial activity, and include examples from the Western Interior Seaway (Kauffman *et al.*, 1996; Metz, 2010; Kiel *et al.*, 2012) and the northern Tethyan and North African continental margins (Layeb *et al.*, 2012, 2014). Limestones from the Western Interior Seaway feature shallow-water methane-seep deposits that formed during OAE 2 in warm bottom waters (Kiel *et al.*, 2012), and are characterized by ^{13}C -depleted carbonate mineral phases and a high-abundance but low-diversity faunal assemblage. The Campanian organic-rich Pierre Shales comprise numerous peculiar carbonate bodies, collectively known as the Tepee Buttes (Shapiro & Fricke, 2002; Metz, 2010). These deposits are rich in chemosymbiotic macrofaunal communities and exhibit diagnostic ^{13}C -depleted mineral fabrics and ^{13}C -depleted molecular fossils of the anaerobic oxidation of methane (AOM) consortium, confirming that carbonate precipitation was driven by microbial oxidation of methane (Kauffman *et al.*, 1996; Birgel *et al.*, 2006). The fossiliferous Tepee Butte limestones possibly formed during periods of enhanced bottom water oxygenation, supported by the presence of molecular fossils of aerobic methanotrophic bacteria (Birgel *et al.*, 2006). Layeb *et al.* (2012) documented carbonate build-ups from the Lower Cretaceous Fahdene Basin in Tunisia. These limestones reveal a thrombolitic fabric and formed within organic-rich black shales deposited during the Late Albian OAE 1d. The fabric and texture of these limestones suggest the involvement of microbes during their formation below a water body with eutrophic, anoxic waters. Layeb *et al.* (2014) further reported on mound-shaped carbonate structures associated with OAE 2 within Late Cenomanian black shales from the Bahloul Formation in Northern Tunisia. The genesis of the Tunisian limestones possibly involved microorganisms mineralizing large amounts of organic matter, as suggested by ^{13}C -depleted carbonate cements and thrombolitic fabrics (Layeb *et al.*, 2014).

This study reports on a large limestone body associated with black shales deposited in the aftermath of OAE 2 exposed along a coastal section of the Tarfaya Basin, Morocco. A combination of petrography, macro- and micropalaeontology, carbon and oxygen stable isotope and trace element geochemistry, as well as lipid biomarkers has been used to decipher the mode of carbonate accretion that led to the unusual morphology of this limestone body. The potential triggers for carbonate precipitation within the mid-Cretaceous organic-rich

deposits, and the impact of the prevailing oceanographic and geochemical conditions on the benthonic environment and faunal communities are assessed. Although the Amma Fatma limestone body reveals only a limited number of lithological features typical of hydrocarbon seep carbonates and apparently no endemic seep fauna, it is shown to have resulted from methane seepage. The lack of obligate, endemic seep fauna is interpreted to have been caused by (1) shallow water depth – a factor known to discriminate against seep taxa (Kiel, 2010) – and (2) the eutrophic palaeoenvironment in the aftermath of OAE 2 that favoured photosynthetic primary production and subsequent consumption of organic matter by heterotrophs. This work reveals that seep deposits are difficult to identify in high productivity settings, where chemosynthesis-based seep fauna is likely to be outcompeted by heterotrophic background fauna.

GEOLOGICAL SETTING

Deposits from the Cenomanian–Turonian (C/T) boundary in Northern Africa have been intensively studied in Tunisia and Morocco. This is partly due to the fact that these regions feature up to 800 m thick successions of organic-rich shales and limestones (Kuhnt *et al.*, 2001; Kolonic

et al., 2002), making them prolific petroleum source rocks (Leine, 1986) and high resolution climate archives (Kolonic *et al.*, 2005; Kuhnt *et al.*, 2005). The southern Moroccan passive continental margin includes the Tarfaya Basin, one of several palaeo-shelf basins located on the coasts of Senegal, Morocco and Tunisia (Figs 1 and 2A; Lüning *et al.*, 2004; Kolonic *et al.*, 2005). It covers an area of around 170 000 km² and features the highest accumulation rates of organic matter from the C/T boundary known to date, as well as one of the largest oil shale deposits in the world (Amblés *et al.*, 1994; Kuhnt *et al.*, 2001). The Tarfaya Basin is situated to the south of the Anti-Atlas Mountains and extends into the Tindouf Basin to the East, the Senegal Basin to the South, and is bordered by the East Canary Ridge to the West (Kolonic *et al.*, 2002). It has been suggested that the basin was a distal section of the proto southern North Atlantic with outer shelf to upper bathyal water depths of 200 to 300 m (Figs 1 and 2B; El Albani *et al.*, 1999b; Kuhnt *et al.*, 2001). It experienced intense upwelling, extended oxygen minimum zones and recurrent pulses of high primary production since at least the Late Cenomanian (Kuhnt & Wiedmann, 1995; El Albani *et al.*, 1999a,b; Kolonic *et al.*, 2002, 2005), leading to pronounced redox cycles on orbital time scales that alternated between sulphidic and anoxic ferruginous water-column conditions (Poulton *et al.*, 2015).

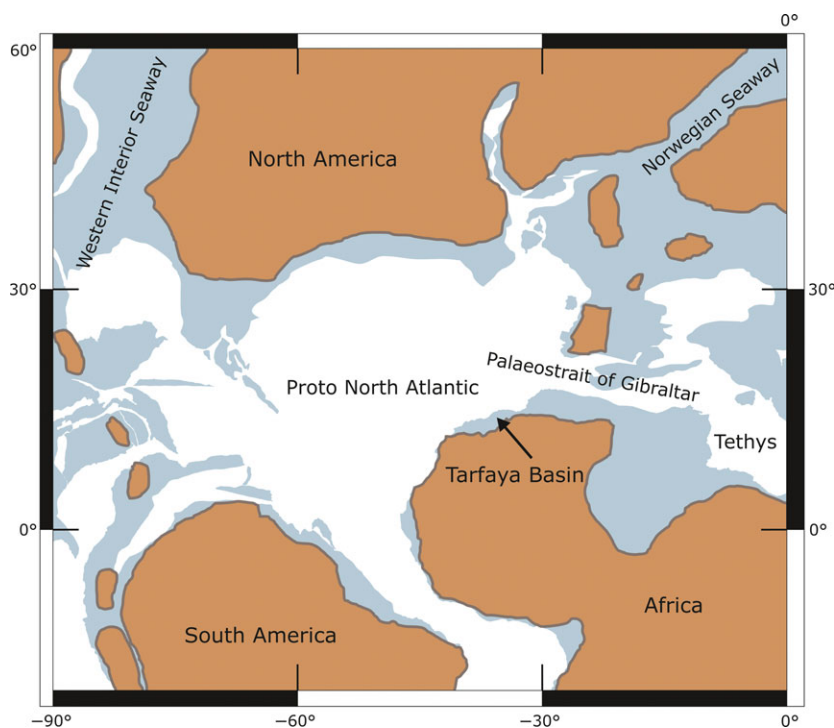


Fig. 1. Palaeogeographical map of the mid-Cretaceous (ca 94 Ma) showing the study site within the Tarfaya Basin, Morocco. Light blue areas represent continental plates covered by shallow epicontinental seas, brown areas represent dry land. Brown, thick lines delineate palaeocoastlines (modified from Kuypers *et al.*, 2002).

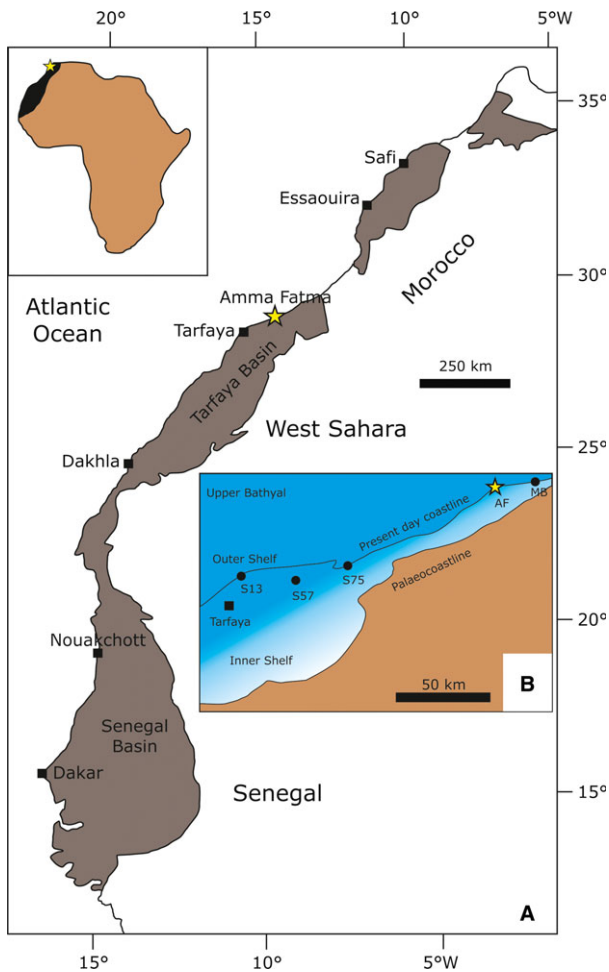


Fig. 2. (A) Locality map showing the distribution of unfolded Mesozoic and Cenozoic Basins containing black shales (grey) from the C/T boundary along the northwestern African continental margin (modified from Kolonic *et al.*, 2005). Yellow stars indicating the Amma Fatma section in (A), (B) and the small inset map in the upper left, which indicates the location of the studied section in Africa. (B) Palaeogeographic map of the Tarfaya Basin (modified from Kolonic *et al.*, 2005); AF = Amma Fatma, MB = Mohammed Plage, S13, S57 and S75 = drill cores described by Leine (1986) and Kolonic *et al.* (2005).

The carbonate body studied here crops out at Amma Fatma Plage, which is a coastal to middle shelf section at the northern edge of the Tarfaya Basin (Fig. 2). Amma Fatma Plage is located *ca* 8 km to the south-west of Mohammed Plage, the latter being a well-studied coastal section of the basin where deposition of organic-rich shales and carbonate beds occurred close to the palaeo-coastline (El Albani *et al.*, 1999b; Kolonic *et al.*, 2005). Both sites experienced a series of transgressive cycles during the mid to late Cretaceous that caused repeated and widespread flooding, and initiated the deposition of laminated biogenic sediments associated with OAE 2

(Kolonic *et al.*, 2002, 2005; Gebhardt *et al.*, 2004; Kuhnt *et al.*, 2009; Gertsch *et al.*, 2010). Amma Fatma Plage lies along a 175 km long palaeotranssect through the Tarfaya Basin, together with shallow exploration wells S13, S57, S75 and Mohammed Plage (cf. Kolonic *et al.*, 2002, 2005). The transect runs in SW to NE direction and connects its deepest and most distal part at wells S13 and S57 to its most proximal part at Mohammed Plage (Fig. 2B). Exploration well S13 is interpreted as an open-marine shelf setting with water depths of 200 to 300 m, whereas Mohammed Plage and Amma Fatma Plage represent shallower, proximal successions deposited at the northwestern margin of the Sahara platform (Kolonic *et al.*, 2002, 2005; Kuhnt *et al.*, 2009).

MATERIAL AND METHODS

Petrography, mineralogy and palaeontology

Rock samples from the carbonate body and from a vertical profile at Amma Fatma Plage were collected during a field trip in 2003. Samples from the studied sedimentary succession were recovered from a fresh coastal exposure in direct proximity to the carbonate body, and taken at regular intervals of 5 to 10 cm across the profile. A total of 20 samples were collected from various zones of the carbonate body, two further samples were collected from a carbonate bank covering the structure (hereafter referred to as cover bed). Thin sections (150 × 100 mm, 100 × 75 mm) were made at the University of Bremen and the University of Vienna. Thin section microscopy was conducted using a Leica DM4500 P polarization microscope (Wetzlar, Germany). Photographs were taken with a Leica DFC 450 C camera using the Leica Application Suite 4.4.0 software. Additionally, a Nikon SMZ 1500 stereomicroscope coupled to a Prog.Res Speed XT core 5 camera, as well as a Nikon Optiphot-2 optical microscope (Tokyo, Japan) were used for petrographic observations using the software Prog.Res Capture pro 2.8 for image analysis and camera control. To discriminate the different carbonate minerals under the microscope, several thin sections were stained with a mixture of potassium ferricyanide and alizarin red S solution dissolved in 0.1% hydrochloric acid (cf. Dickson, 1966). Powdered samples for X-ray diffraction (XRD) and carbon and oxygen stable isotope analyses were obtained from polished rock slabs using a hand-held microdrill at low to medium rotational speed. For XRD analysis, powdered samples were analysed with a Panalytical PW 3040/60 X'Pert PRO (CuK α radiation, 40 kV, 40 mA, step size 0.0167.5 s per step) diffractometer at the University of Vienna. X-ray diffraction patterns were interpreted using the Panalytical software "X'Pert High score plus". Calcareous nannoplankton

assemblages were studied in 150 samples with a high-resolution spacing of about 4 to 7 cm within the slabbed intervals. For the calcareous nannoplankton, smear slides were prepared using techniques described in Bramlette & Sullivan (1961) and Hay (1961, 1965). The slides were examined at a magnification of about 1250 times under both cross-polarized and phase-contrast illumination.

Inorganic geochemistry – Total organic carbon, carbon and oxygen stable isotopes and trace elements

Total carbon (TC) and total organic carbon (TOC) contents of the Amma Fatma carbonate body were determined using a LECO RC-612 Carbon Analyzer (St. Joseph, MI, USA), equipped with a solid-state infrared detector at the Department of Environmental Geosciences at the University of Vienna. All samples were ground to fine powder in an agate mortar prior to measurements. To measure TC, carbon dioxide was released at a temperature of 1000°C. Prior to sample measurements a pure CaCO₃ standard (Co. Merck, Kenilworth, NJ, USA) was measured, revealing a relative standard deviation of 0.06%. The TOC contents were determined at 550°C. A Synthetic Carbon Leco 502-029 (1.01 ± 0.02 carbon%) standard was measured prior to sample analyses and a standard deviation of 0.005% was calculated. Carbonate (CaCO₃%) contents were calculated according to the equation: CaCO₃% = (TC – TOC) × 8.333. All black shale samples were carefully dried and ground in an agate mortar. The TIC and TOC contents of black shales were measured using a LECO CS-300 carbon-sulphur analyser at the Geoscience Department, University of Bremen. Before TOC determination, inorganic carbon was carefully removed by repetitive addition of 0.25 N HCl. The CaCO₃ contents were calculated as above (precision of measurements ±3%). The δ¹³C_{TOC} values (±0.1‰ vs. Vienna Pee Dee belemnite, V-PDB) were determined on decalcified sediment samples using automated on-line combustion followed by conventional isotope-ratio mass spectrometry.

A total of 48 sample powders from 12 different samples throughout the Amma Fatma carbonate body were analysed for their stable carbon and oxygen isotope content. Sample powders were obtained from polished rock slabs using a hand-held microdrill. Stable carbon and oxygen isotope analyses were performed at the light stable isotope laboratory of the Institute of Earth Sciences, Karl-Franzens University, Graz. Effective accuracy was ±0.05 for δ¹³C values and ±0.11 for δ¹⁸O values. The δ¹³C and δ¹⁸O values are reported relative to V-PDB (standard deviation smaller than 0.04‰), and appropriate correction factors were applied.

Trace metal compositions of black shales and limestones were determined using X-ray fluorescence (XRF) spectrometry on fused-borate glass beads, and by inductively coupled plasma atomic emission spectrometry (ICP-AES). The XRF calibration curves were based on international standard reference material. For ICP-AES, about 50 mg of sample powder was digested in a mixture of 3 ml HNO₃ (65%), 2 ml HF (40%) and 2 ml HCl (36%) of suprapure quality at 200°C and 30 kbar in closed Teflon vessels (Heinrichs *et al.*, 1986). Sample powders were then dried by evaporation, and the residue was re-dissolved in 0.5 ml HNO₃ (65%) and 4.5 ml deionized water. The solutions were analysed with ICP-AES, and the results were checked with international standard reference material. Relative standard deviations in duplicate measurement were below 3%. Enrichment factors (EFs) of trace elements were calculated according to Brumsack (2006):

$$EF_{\text{element}} = (\text{element}/\text{Al})_{\text{sample}} / (\text{element}/\text{Al})_{\text{average shale}}$$

Average shale refers to the composition of collected shale samples compiled by Wedepohl (1969). An element with an EF either above or below 1 is considered to be enriched or depleted compared to average shale, respectively.

Organic geochemistry – Lipid biomarkers

Four carbonate rock samples were chosen for biomarker analysis, one from the cover bed and one from each of the zones 4, 3 and 1. The samples were cleaned repeatedly by washing with 10% hydrochloric acid (HCl) and then dichloromethane (DCM) to avoid any contamination, and then ground to fine powder. All carbonates were treated with a 'two-step extraction procedure' to discriminate preferentially intercrystalline-bound from preferentially intracrystalline-bound molecular fossils (cf. Thiel *et al.*, 1999; Guido *et al.*, 2013), and to separate compounds tightly associated with the carbonate matrix from easily extractable compounds. To obtain preferentially intercrystalline-bound compounds, the ground samples were extracted by ultrasonication in DCM : MeOH (3 : 1) nine times until the solvents became colourless to get the first total lipid extract (TLE). This extract is referred to as the extract before decalcification below. To obtain preferentially intracrystalline-bound molecular fossils, the residual sediment of the first extraction step was decalcified and then extracted again. In detail, doubly distilled water was added and 10% HCl was slowly poured onto the samples. To avoid transesterification reactions at low pH, HCl addition was stopped when *ca* 75% of the carbonate was dissolved. The remaining sample powder was centrifuged and extracted as described above to

obtain a second TLE. This extract is referred to as the extract after decalcification below. From here on, the extracts before and the extract after decalcification are treated in the same fashion. After washing with clean water, the samples were saponified with 6% potassium hydroxide (KOH) in methanol (MeOH) to release bond carboxylic acids. The supernatants were decanted and the residues were subsequently extracted via ultrasonication in DCM/MeOH (3 : 1; v : v) four times until the solvents became colourless. The combined extracts were then treated with 10% HCl to transfer the free fatty acids (FAs) to the organic solvent phase. For gas chromatography (GC) analyses the extracts were dried with sodium sulphate and the TLE of both extraction procedures were separated by column chromatography. Alcohols were derivatized by adding 100 μ l pyridine and 100 μ l N,O-bis(trimethylsilyl)trifluoroacetamide (BSTFA) to the alcohol fraction at 70°C for 30 min. The derivatized fraction was dried under a stream of nitrogen (N₂) and dissolved in *n*-hexane prior to injection. The alcohol fractions are not described below due to the lack of pristine compounds. Free carboxylic acids were reacted with 1 ml 14% boron trifluoride (BF₃) in MeOH at 70°C for 1 h to form FA methyl esters. After cooling, the mixture was extracted four times with 2 ml *n*-hexane. Combined extracts were evaporated under a stream of N₂ and redissolved in *n*-hexane before injection. The derivatized carboxylic acid fractions were analysed using GC-mass spectrometry (GC-MS) with an Agilent 7890 A GC system coupled to an Agilent 5975C inert MSD mass spectrometer. Quantification was done using GC-flame ionization detection (GC-FID) with an Agilent 7820 A GC system. Internal standards used were 5 α -cholestanol for the hydrocarbon and 2-Me-C₁₈ FA for the carboxylic acid fractions. Both GC systems were equipped with HP-5 MS UI fused silica columns (30 m \times 0.25 mm i.d., 0.25 μ m film thickness). Helium was used as the carrier gas. The GC temperature program for hydrocarbons and carboxylic acids was 60°C (1 min) to 150°C at 10°C min⁻¹, then to 320°C (held 25 min) at 4°C min⁻¹. Compound assignment was based on retention times and published mass spectra.

Compound-specific stable carbon isotope analysis was performed using a Thermo Fisher Trace GC Ultra connected via a Thermo Fisher GC Isolink interface to a Thermo Fisher Delta V Advantage spectrometer at the Department of Terrestrial Ecosystem Research, University of Vienna. Compound-specific carbon isotope values are given as δ values in per mil (‰) relative to V-PDB. The $\delta^{13}\text{C}$ values of carboxylic acids (methyl esters) were corrected for additional carbon introduced after derivatization. Each measurement was calibrated using several pulses of carbon dioxide (CO₂) of known isotopic composition prior to and after the run. Precision was checked

with an *n*-alkane mixture (C₁₄ to C₃₈) of known isotopic composition. Analytical standard deviation was <0.7‰.

RESULTS

Amma Fatma section – Lithology, biostratigraphy and inorganic geochemistry

The complete section at Amma Fatma Plage measures ca 14 m from top to bottom and features cyclic alternations of black shales, siltstones and organic-rich, marly limestone beds (Figs 3 and 4). The limestones are represented by (1) carbonate nodules mainly composed of mudstones and wackestones that are aligned parallel to stratification and (2) discontinuous bioclastic storm beds with hummocky cross-stratification (cf. El Albani *et al.*, 1999b). The limestones contain Foraminifera, calcispheres, molluscs including ammonites, brachiopods, variable amounts of quartz grains and are partly bioturbated. A detailed microfacies analysis is included in El Albani *et al.* (1997, 1999a). The succession of 22 beds is shown by the stratigraphic chart of the outcrop in Figs 3 and 5. Limestone and black shale beds alternate regularly, whereby their thicknesses measure 20 to 80 cm and 60 to 300 cm, respectively. Beds comprising limestone nodules with chert measure up to 20 cm in thickness. One exception is a 1 m thick bed 3 m above the base of the profile featuring large carbonate nodules with a corona made of chert. Calcium carbonate and TOC contents of the black shale beds vary from 60 to 90% and 4 to 9%, respectively. Calcium carbonate and TOC values throughout the section are shown in Table 1. The characteristic positive $\delta^{13}\text{C}_{\text{TOC}}$ excursion that is prominently observed across the C/T boundary in adjacent sites is not found at Amma Fatma Plage, supporting a post OAE period of deposition. The measured $\delta^{13}\text{C}_{\text{TOC}}$ values vary slightly between -26.2 and -27.8‰.

Biostratigraphic data confirm the positioning relative to the OAE 2 carbon isotope excursion, placing the investigated sedimentary succession within the *H. helvetica* planktonic foraminiferal zone and the *coloradoense* and *nodosoides* ammonite zone of the upper part of the Lower Turonian stage (cf. Marzouk & Lüning, 2005). The position of the nannofossil zonal datum marker CC11/CC12 is placed at about 9.5 m above the *helvetica* and *nodosoides* zones. Planktonic Foraminifera are present in very high numbers and benthonic foraminiferal faunas are of low diversity. A highly diverse and highly abundant calcareous nannofossil flora was observed in all samples studied. Preservation is moderate, except in the uppermost part of the section (from 13.5 m onwards), where preservation is good. *Watznaueria barnesae* and *Eiffelithus turrisseffilii* are abundant throughout the section (except

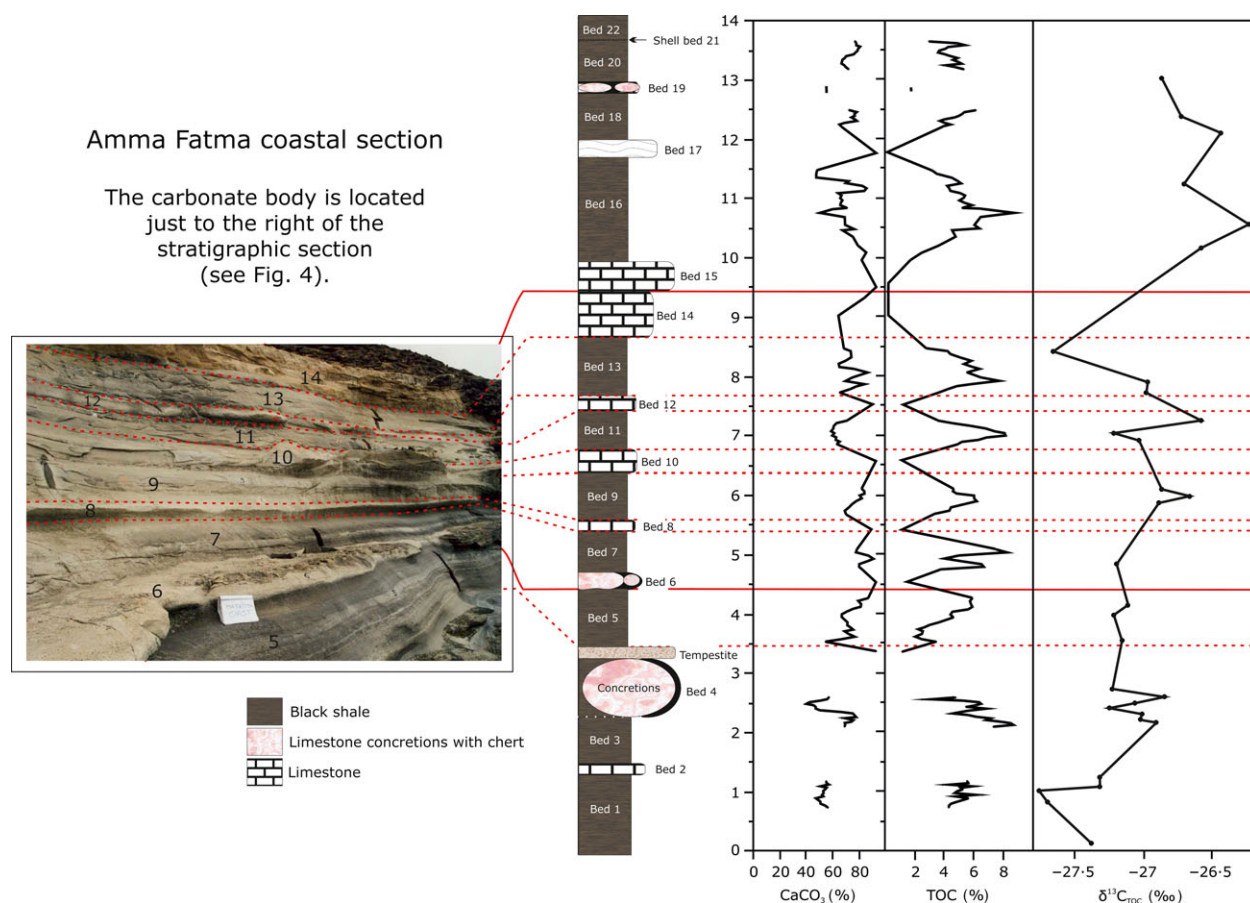


Fig. 3. (Left) Photograph of the Amma Fatma outcrop section showing beds 5 to 14 separated by dashed red lines; the Amma Fatma carbonate body lies within beds 6 to 14 delimited by the thick red lines (cf. Fig. 4). (Centre) Lithostratigraphic chart of the Amma Fatma coastal section showing lithologies and their corresponding thickness. (Right) CaCO₃ content, total organic carbon (TOC) content and its carbon stable isotope composition within the corresponding beds.

in two carbonate beds), and are known to be very resistant to solution. Although frequent, the abundance of *Watznaueria barnesae* does not surpass 40%, a cut-off value proposed by Roth & Krumbach (1986) to indicate that nannofossil distribution patterns can still largely be used for palaeoecological interpretations, despite diagenetic and syndepositional dissolution. Notably, *Cyclagelosphaera margerelii* shows a similarly abundant distribution and, therefore, appears to be also solution resistant.

The nannofossil distribution in the Amma Fatma section is characterized by many species having longer term, gradual changes, with only some species exhibiting stronger, high-frequency abundance fluctuations over a few centimetres (*Tranolithus orionatus*, *Zeugrhabdus diplogrammus*). Abundant species throughout the section include *Zygodiscus erectus*, *Rhagodiscus splendens* and *Eprolithus floralis*. *R. splendens* occurs in moderate and high abundances in the lowermost and uppermost parts of the studied section, and is absent in the interval in-

between. Notably, the distribution of *E. floralis* in the section is characterized by similar abundance peaks at the base and top of the section. Other identified species *Broinsonia* spp. (except *B. enormis*) and *Gartnerago* spp. (Thierstein, 1976; Hattner *et al.*, 1980) are notably rare throughout the section. An exception is a *Gartnerago segmentatum* abundance peak between 7.5 and 8 m. Abundance and distribution of all identified nannofossil species and phosphorus content throughout the Amma Fatma section are shown in Fig. 5.

Total contents of all measured elements are shown in Table 1. Prominent trace metal enrichment is restricted to stratigraphic intervals that correspond to the organic carbon-rich black shales. Trace metal patterns vary across the section between alternating black shales and limestone beds, and also within the black shale successions themselves. Calculated EFs of trace metals whose deposition is influenced by bottom and pore water redox conditions are plotted with depth in Fig. 6. Mean trace metal

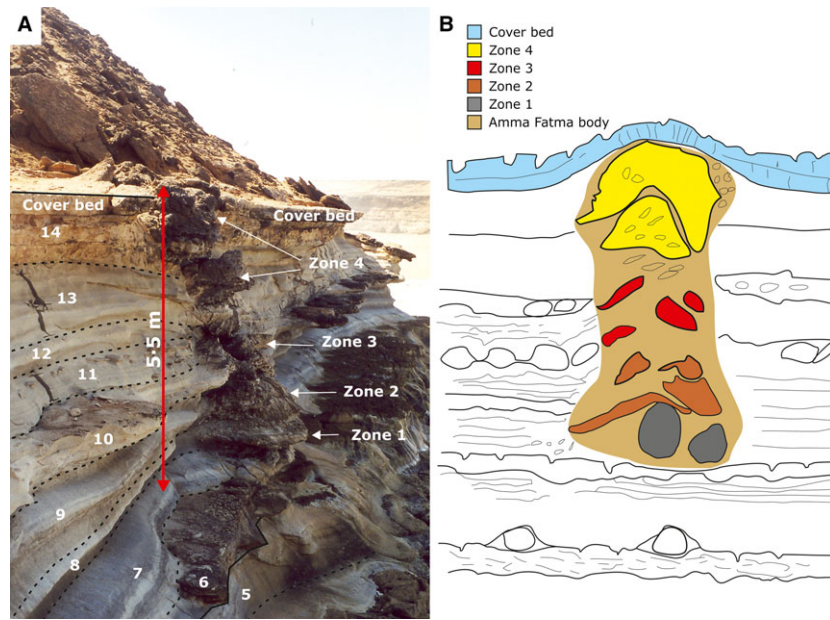


Fig. 4. (A) Photograph of the Amma Fatma carbonate body with its four zones highlighted by arrows amongst the beds shown in Fig. 3. (B) Schematic sketch of the Amma Fatma body highlighting the four zones from bottom to top and the cover bed capping the body.

concentrations and EFs of black shale and limestone beds that correspond to zones 1 to 4 and the cover bed are shown in Tables 2 and 3, respectively. Zone 1 shows the lowest concentration of several major elements including Al, Mg, Fe and Mn (Tables 1 and 2). Particularly, zone 1 has an Al content that is half that of zone 4, which has a considerable effect on calculated EFs. Zone 4 reveals relatively high Al contents, and all EFs are higher in the lower zones 1 and 2 compared to zone 4 (Table 3). As EFs may be exaggerated due to varying Al content, they must be considered together with absolute contents of the respective elements. This is particularly the case for bed 14, which consists mainly of marly limestone and exhibits low Al concentrations. Chromium, Co and U are the only trace metals whose concentrations increase from zone 1 to 4 (Table 2), whereas Mo concentrations in zone 1 and 4 are almost equal. There is a distinct peak of all trace metals except Cr and Co in zone 3, which is not as apparent in respective EFs due to high Al contents in this zone. Bed 14 exhibits the lowest contents of most trace metals with the exception of U. Molybdenum/U ratios decrease steadily from bottom to top and fall below unity in bed 14. Correlation coefficients between trace metals and Al, as well as between trace metals themselves were calculated and are shown in Table 4. The only trace metals that exhibit correlation with Al are Cr and Co, with the latter correlated better than the former. Trace metal correlations can be distinguished into three groups of elements that correlate well among each other, these being

(1) Cr with Cu, (2) Mo with Ni, Zn and V and (3) Zn with Ni and Cd (Table 4).

The Amma Fatma carbonate body

The carbonate body associated with black shales (Figs 3 and 4) is enclosed by beds 6 to 14 of the Amma Fatma section, and measures 5.5 m in height and 3.6 m in width. The carbonate body was divided into 4 zones, illustrated in a schematic sketch (Fig. 4B). Zones 1 and 2 comprise the base and lowermost part of the structure and feature concretionary and nodular carbonates penetrated by numerous veins made of secondary precipitates (Fig. 7). A carbonate bank measuring 17 to 19 cm in thickness separates zone 1 from 2 (Fig. 7B). Zone 3 comprises the middle part of the body, and features massive limestone blocks and nodules. Zone 4 is the topmost part of the carbonate body and yielded abundant molluscan fossils, as well as cylindrical to tubular trace fossils (Fig. 8C). The top of the body is capped by a 15 to 20 cm thick carbonate bank, referred to as a cover bed (Figs 4 and 8A to C), which corresponds to bed 14 of the section (Figs 3 and 4A).

The Amma Fatma carbonate body – Petrography and mineralogy

Micrite (i.e. microcrystalline calcite with a crystal size below 10 μm) is the dominant primary mineral that

Table 1. Total concentrations of all measured elements of the Amma Fatma black shale section. All data are given in ppm except depth (in m), CaCO₃ and total organic carbon (TOC) content (both in %)

Depth [m]	CaCO ₃ [%]	TOC [%]	Ti	Al	Ba	Ca	Fe	K	Mg	Mn	P	Cr	Mo	Ni	Zn	Cu	V	Pb	As	Cd	Co	Re	U
13.5	10.0	3.62	342	6342	664	293 386	2946	3567	9149	41.7	716	286	103	44.6	40.2	10.6	93.1	2.07	7.19	1.36	1.97	0.050	9.93
13.4	34.6	5.66	426	6792	43.7	279 035	3381	4069	8796	35.0	528	353	22.6	67.5	139	13.7	154	2.04	7.13	2.55	2.00	0.100	9.05
13.3	18.9	4.13	501	8446	52.3	284 508	4474	4613	10 626	46.1	438	345	20.7	53.8	75.5	10.7	183	1.76	7.38	2.14	2.12	0.040	8.73
13.1	19.9	5.47	614	11 928	60.6	252 778	6346	5416	9189	44.7	1419	40.8	23.9	63.1	79.8	11.6	206	2.42	9.41	2.10	2.51	0.060	9.15
13.0	27.7	5.59	421	9278	54.3	264 626	4559	4146	7795	38.4	1103	46.6	23.4	62.4	111	12.7	192	2.32	8.87	3.03	1.95	0.050	8.01
12.9	19.5	2.51	1158	15 361	81.5	211 050	8242	7054	16 448	81.5	735	434	23.3	59.8	78.3	11.3	246	3.12	9.04	1.76	3.13	0.020	6.14
12.4	36.4	6.28	550	9047	57.7	263 207	4937	4656	9411	42.4	724	40.6	26.4	78.0	146	13.4	161	2.59	7.31	3.12	2.27	0.110	8.47
12.3	33.3	5.32	473	7043	60.0	276 795	2912	4008	8186	36.3	613	39.7	13.2	55.8	133	11.9	106	2.11	7.11	2.80	1.97	0.060	8.99
12.1	29.7	4.37	833	11 564	64.2	243 988	5638	5432	14 622	58.9	522	46.1	22.7	68.8	119	15.4	160	2.95	9.22	2.39	2.49	0.090	9.39
11.7	2.7	0.231	60.0	967	85.2	363 527	523	513	3699	38.4	122	461	3.00	6.89	10.7	1.90	38	1.04	3.06	1.02	1.06	0.020	0.756
11.2	28.8	3.78	1786	22 793	108	188 394	11 925	9355	18 824	102	612	588	18.6	56.0	115	15.5	185	4.30	15.1	2.67	4.58	0.030	5.54
11.1	37.6	5.43	1065	13 377	82.4	240 279	6123	6743	14 798	70.0	633	539	17.1	54.5	150	17.5	170	3.31	11.4	4.96	2.72	0.040	7.96
10.9	21.2	5.67	1066	14 505	88.5	253 042	6787	6767	12 459	66.6	830	62.2	13.2	45.7	84.9	18.0	127	3.22	11.9	1.70	3.06	0.050	6.34
10.8	28.4	6.07	1006	13 631	85.0	251 781	5493	6760	13 487	65.9	616	593	8.54	52.3	114	15.3	97.7	2.73	10.3	2.25	3.05	0.040	5.07
10.7	49.1	6.54	793	12 000	72.1	234 427	6510	5709	12 893	65.3	505	639	18.9	82.6	197	23.0	160	4.00	13.3	3.89	3.13	0.060	9.04
10.6	47.4	6.46	647	9490	63.3	244 942	4457	4428	10 286	49.0	557	51.9	15.9	73.2	190	18.4	135	3.06	10.8	3.96	2.48	0.030	9.58
10.4	34.0	5.09	785	10 620	76.2	229 982	4745	5950	17 944	60.0	469	469	9.46	56.7	136	12.1	86.2	2.89	12.4	2.97	2.45	0.030	7.31
10.2	14.0	2.37	597	7754	53.4	245 794	3220	4770	30 725	70.2	262	21.7	3.57	26.5	55.9	8.11	31.8	1.54	7.68	1.37	2.13	0.020	6.39
9.91	3.48	0.068	116	1695	76.5	346 508	781	1229	6814	31.5	131	661	3.44	5.30	13.9	3.08	13.8	1.17	11.5	1.38	1.13	0.040	1.86
9.35	3.62	0.093	170	2556	37.7	303 607	548	1959	8324	27.7	142	182	2.27	5.86	14.5	5.66	48.3	1.56	5.67	1.83	1.14	0.030	5.20
8.67	11.3	0.064	498	7031	55.6	279 359	3260	3950	14 793	54.0	609	31.6	5.18	19.2	45.2	5.22	127	3.27	9.52	3.07	2.90	0.030	6.37
8.39	21.9	3.45	918	13 497	80.8	239 388	6821	5831	23 383	75.9	613	41.1	13.0	42.5	87.7	11.9	150	2.77	13.0	1.47	2.67	0.020	6.41
8.20	31.7	6.03	779	11 637	76.1	242 917	5315	5620	19 351	59.6	683	595	19.1	52.9	127	24.6	148	2.99	11.6	1.62	2.29	0.050	7.67
8.07	21.8	6.51	602	9544	79.3	268 301	3827	4640	9738	43.7	825	51.0	19.2	47.4	87.2	16.5	135	2.69	8.86	1.60	1.90	0.040	9.77
7.87	25.1	7.63	526	10 743	96.0	259 113	4782	4902	8169	41.0	688	597	23.6	55.2	101	19.2	167	3.14	10.7	1.69	2.09	0.040	10.1
7.8	17.9	5.20	452	6305	55.8	289 013	2794	3134	7930	36.4	583	382	13.1	40.2	71.6	13.2	98.8	2.10	7.82	1.64	1.74	0.020	7.87
7.69	15.4	4.15	995	14 670	81.4	236 752	6152	5843	18 177	68.2	426	537	10.8	32.1	61.7	13.0	107	3.10	9.98	1.52	2.56	0.040	5.61
7.45	10.8	1.17	485	7054	134	301 984	2927	3015	9045	43.0	197	191	6.01	14.0	43.3	6.67	57.5	2.01	7.05	1.32	1.55	0.002	2.40
7.22	21.3	4.08	846	11 967	84.7	277 504	4594	4909	10 053	52.9	695	46.0	10.6	44.9	85.2	11.8	121	2.48	8.63	5.10	2.87	0.030	5.95
7.13	43.4	5.94	1029	14 959	85.1	245 875	7350	5747	9414	54.0	930	55.8	25.1	85.5	174	19.8	247	4.03	11.9	4.87	3.62	0.080	9.35
7.00	90.3	8.00	969	13 749	79.2	243 523	6853	5450	9233	49.5	1122	593	36.7	122.0	361	25.0	403	4.27	12.3	8.24	3.55	0.150	12.2
6.94	70.9	6.45	972	14 450	80.3	246 417	7215	5654	11 185	54.8	857	55.0	31.4	99.2	284	20.3	322	4.21	12.6	6.89	3.42	0.220	9.57
6.88	44.3	5.26	1057	15 136	85.1	247 997	7506	5896	13 140	59.3	1083	55.5	25.4	78.6	177	17.4	254	4.46	13.0	4.32	3.23	0.160	9.70
6.5	5.5	1.00	220	3212	39.5	354 767	1272	1392	5525	40.7	199	11.9	3.74	12.6	22.1	4.29	64.6	1.54	4.88	1.42	1.38	0.020	1.97
6.05	23.2	4.96	422	6315	58.2	303 839	2701	3090	7409	35.6	610	38.2	13.9	52.6	92.9	12.5	88.2	2.53	7.17	2.56	2.16	0.060	7.66
5.93	33.0	6.34	570	8509	61.6	291 161	3829	3824	7684	41.8	550	36.4	15.7	63.4	132	14.7	108	3.14	7.80	3.29	2.31	0.050	6.48
5.82	29.5	4.77	920	13 799	82.0	260 758	6191	5599	14 255	66.6	515	49.1	16.8	53.3	118	13.8	121	3.19	11.1	3.01	3.04	0.030	5.20
5.44	11.7	1.12	509	7378	107	312 712	3433	3224	9423	50.9	250	19.5	5.40	17.2	46.8	5.33	40.4	2.13	6.66	1.90	2.27	0.020	1.70
4.92	61.2	8.09	351	5401	55.4	300 061	2429	2891	8959	32.0	753	48.6	22.7	96.5	245	16.0	173	3.25	7.90	5.75	2.18	0.060	8.54
4.85	38.0	4.48	251	4097	44.5	330 172	1950	2190	7617	31.7	574	38.8	16.9	62.5	152	11.2	161	2.72	5.43	4.80	1.96	0.050	6.80
4.78	72.8	6.73	467	7096	58.7	296 750	3893	3377	10 794	45.8	956	45.1	28.3	94.6	292	15.9	231	3.34	8.76	7.55	2.50	0.050	7.76

(Continued)

Table 1. Continued.

Depth [m]	CaCO ₃ [%]	TOC [%]	Ti	Al	Ba	Ca	Fe	K	Mg	Mn	P	Cr	Mo	Ni	Zn	Cu	V	Pb	As	Cd	Co	Re	U
4.75	37.1	4.29	506	7904	61.0	304 941	3895	3588	12 375	53.6	662	37.1	19.8	64.1	149	11.9	194	3.08	6.95	5.29	2.39	0.050	5.96
4.55	14.7	1.46	193	3026	56.0	336 650	1400	1634	6612	41.6	358	15.2	3.67	18.5	59.0	4.98	83.2	2.24	4.18	1.72	1.51	0.020	2.54
4.23	37.4	6.10	423	6121	66.4	307 471	2695	2839	7314	33.8	704	41.1	14.2	63.9	150	13.2	124	2.79	7.10	4.57	2.14	0.050	8.24
4.08	29.1	6.10	549	8718	63.0	294 824	3456	3196	7015	33.8	482	40.6	19.0	51.0	117	13.5	150	3.79	8.14	3.02	2.02	0.020	7.12
3.91	36.0	5.01	918	13 538	77.5	258 689	6963	4864	14 672	61.5	604	46.6	21.4	61.4	144	13.8	199	3.67	11.2	4.18	2.93	0.050	6.93
3.62	17.9	3.20	1139	16 723	92.1	280 049	8198	5923	13 293	81.8	504	41.1	14.0	39.9	71.5	12.1	157	3.20	12.9	2.04	3.02	0.010	5.16
3.48	20.6	4.02	1623	23 868	124	209 749	11 962	8254	16 204	93.5	501	80.6	16.2	44.7	82.5	15.4	190	4.00	17.0	2.13	4.05	0.040	5.41
3.14	5.70	1.05	335	4713	124	348 899	2432	1764	7141	40.0	198	13.3	4.46	15.0	22.8	4.10	78.4	1.81	5.71	0.98	1.56	0.020	1.64
2.65	37.8	5.11	1130	16 500	94.2	222 161	8856	6632	15 091	68.3	730	43.7	27.0	73.3	151	16.1	362	4.11	13.8	3.60	3.32	0.030	7.12
2.62	37.9	3.75	888	13 315	81.0	220 796	6738	5278	12 784	58.9	628	35.1	21.4	58.7	152	12.2	296	3.05	10.4	2.79	2.82	0.060	5.86
2.52	57.1	6.61	1557	22 446	114	169 364	12 514	8565	17 283	82.3	974	55.7	35.1	84.4	229	19.3	428	4.76	18.7	6.54	4.18	0.110	9.49
2.47	56.9	5.75	1508	21 271	117	180 611	11 811	8226	16 347	80.2	846	71.7	37.5	84.5	228	18.6	414	4.61	18.4	4.93	4.20	0.030	9.19
2.42	59.3	6.90	1405	20 537	112	180 636	10 620	7893	15 405	70.7	850	55.3	36.7	84.6	238	20.2	389	5.03	17.5	4.93	3.90	0.030	8.98
2.33	29.6	4.99	652	8907	92.3	272 670	4273	4067	10 505	47.3	706	35.4	18.3	44.1	118	11.3	198	2.90	8.26	2.23	2.05	0.050	6.57
2.23	41.7	6.90	624	9153	75.6	268 239	4562	3946	7994	44.6	849	37.5	29.6	67.6	167	16.7	222	3.49	9.78	3.75	2.06	0.070	9.17
2.14	52.1	8.47	649	10 269	74.0	257 396	4016	4293	6995	35.9	510	47.5	30.8	88.5	208	18.6	267	3.22	10.0	4.38	2.34	0.070	8.37
2.09	52.1	7.33	672	10 629	76.6	257 256	39	4515	7951	38.8	484	48.6	22.4	78.4	209	16.6	244	3.21	10.7	3.75	2.27	0.090	8.40
1.24	59.0	5.83	1333	20 823	101	199 540	10 035	6974	19 995	71.9	621	62.8	31.4	67.9	236	18.1	332	4.53	14.6	5.21	3.49	0.010	5.46
1.18	42.6	4.81	1424	22 475	103	203 908	10 222	7184	18 097	65.7	466	59.1	25.1	53.5	170	17.0	299	4.92	17.4	2.80	3.40	0.002	4.49
1.15	87.1	6.10	1479	23 513	108	186 148	11 410	7741	22 088	80.7	722	65.3	36.9	85.6	349	20.0	380	5.02	16.6	7.03	4.18	0.020	6.54
1.02	53.9	5.09	1534	24 136	109	192 277	11 533	7682	19 396	75.2	513	65.4	27.6	71.5	216	18.0	306	4.88	16.9	5.01	4.24	0.020	5.31
0.990	71.5	6.32	1459	23 156	105	186 532	10 952	7669	21 246	75.9	651	63.8	34.9	82.0	286	19.9	343	4.98	16.2	6.46	3.86	0.030	6.20
0.960	42.0	5.15	1538	23 965	109	193 622	10 423	7714	19 272	73.0	473	66.2	30.6	72.6	168	19.1	299	4.99	17.7	3.38	4.39	0.030	5.48
0.920	35.5	5.87	1708	26 651	116	156 833	12 810	8534	20 359	80.0	554	53.4	25.2	68.0	142	16.5	274	4.24	16.3	3.22	3.83	0.040	7.99
0.730	21.5	4.75	1428	21 727	107	184 326	11 082	6854	13 574	72.0	1329	54.8	10.0	47.4	86.0	14.8	106	3.11	12.2	1.70	3.08	0.020	9.73
0.030	44.9	4.43	1148	16 750	89.4	207 076	6587	5357	9817	57.9	440	67.20	28.76	86.6	180	23.2	302	5.74	22.3	4.27	4.70	0.040	6.71

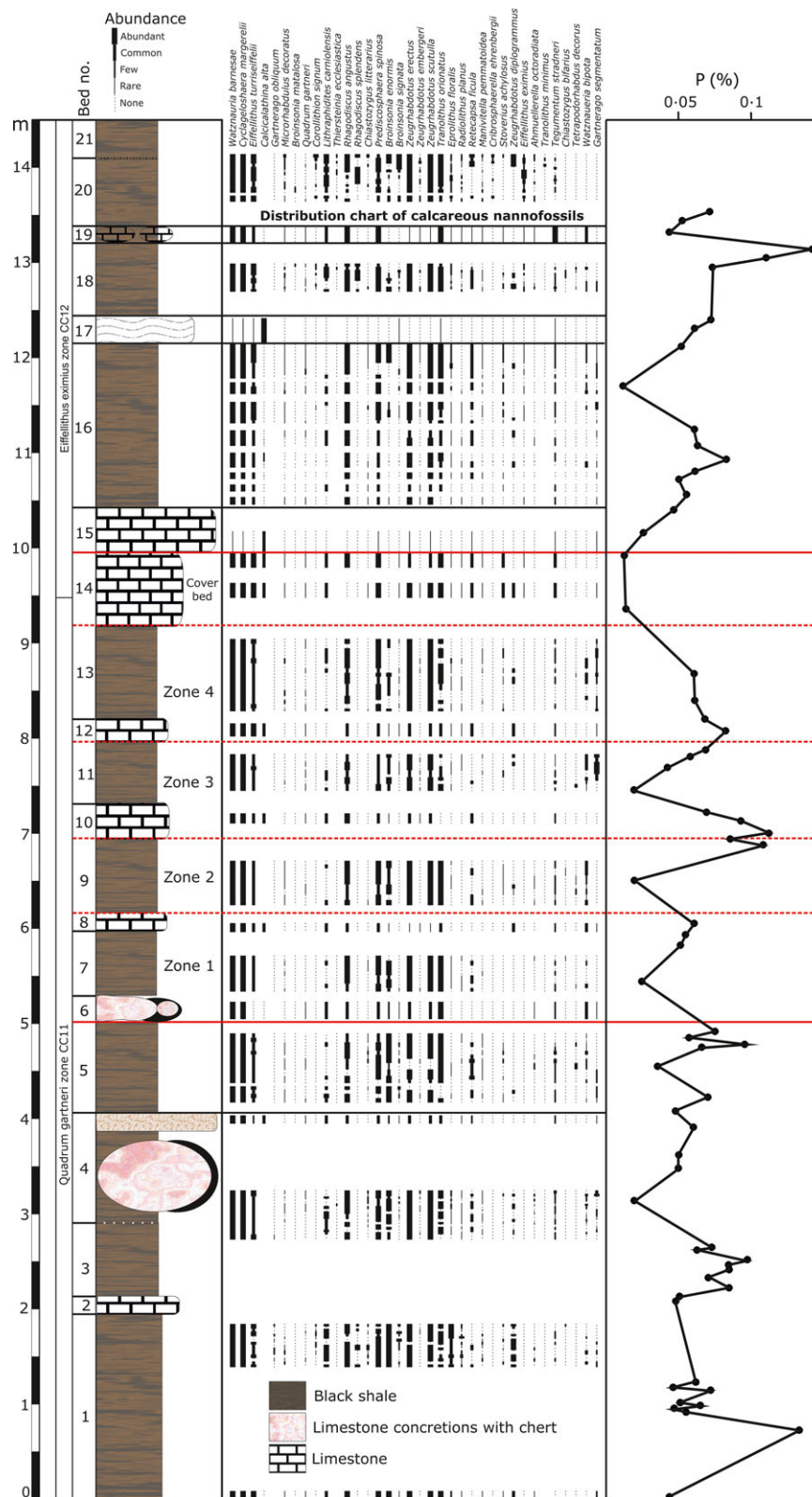


Fig. 5. Distribution chart of nannofossils and phosphorus content across the Amma Fatma section. Solid red lines delineate upper and lower boundaries of the Amma Fatma carbonate body; dashed red lines outline zones 1 to 4 and the cover bed (cf. Fig. 4).

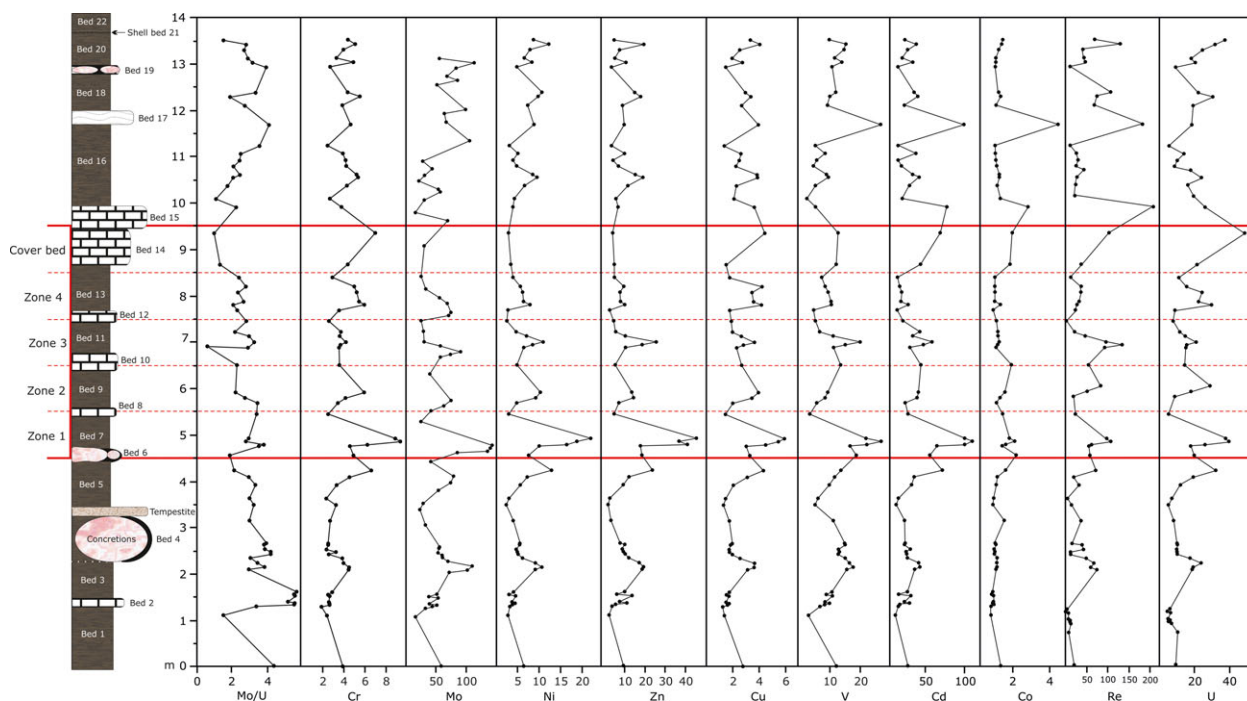


Fig. 6. Trace metal enrichment factors and Mo/U ratios across the Amma Fatma section. Solid red lines delineate upper and lower boundaries of the Amma Fatma carbonate body; dashed red lines outline zones 1 to 4 and the cover bed (cf. Fig. 4, 5).

Table 2. Mean element concentrations in ppm of black shale beds. The stratigraphically corresponding zones of the carbonate body are indicated for comparison

Beds	Zone	Al	Cr	Mo	Ni	Zn	Cu	V	Cd	Co	Re	U	P	Mo/U
14	Cover bed	4794	24.9	3.72	12.5	29.9	5.47	87.4	2.45	2.02	0.030	5.78	376	0.625
13	4	11 066	50.5	16.5	45.1	89.3	16.4	134	1.59	2.21	0.035	7.91	636	2.07
10 to 12	3	11 504	43.2	19.9	65.2	164	15.0	210	4.60	2.81	0.095	7.30	726	2.54
9	2	9541	41.2	15.5	56.5	114	13.6	106	2.96	2.50	0.047	6.45	558	2.49
6 to 8	1	5817	34.0	16.1	58.9	157	10.9	147	4.50	2.13	0.042	5.55	592	2.79

Table 3. Mean major and trace element enrichment factors of black shale beds. The stratigraphically corresponding zones of the carbonate body are indicated for comparison

Beds	Zone	Cr	Mo	Ni	Zn	Cu	V	Cd	Co	Re	U
14	Cover bed	5.67	27.5	3.25	5.61	2.90	12.5	63.4	1.99	70.4	35.0
13	4	4.69	54.3	5.69	7.95	3.09	8.63	17.2	0.956	28.7	18.7
10 to 12	3	3.60	53.7	6.71	11.8	2.50	11.9	43.1	1.22	64.2	14.5
9	2	4.52	59.4	8.48	12.0	3.06	8.00	37.1	1.29	51.5	18.6
6 to 8	1	6.06	94.6	13.6	26.0	3.85	18.2	87.9	1.81	67.5	24.4

makes up the matrix of the Amma Fatma carbonate body. Matrix micrite and peloidal micrite occur, whereby the former is the most abundant carbonate phase in zones 1 and 2, making up at least 80% of the bulk rock volume (Figs 9 and 10A). Matrix micrite is light to dark brown

in colour, exhibits a very heterogeneous and partly clotted texture and is rich in detrital material comprising large amounts of recrystallized bivalve and gastropod shell fragments (Fig. 9A), benthonic Foraminifera (Fig. 9B), *Palaxius* faecal pellets (Fig. 10B), radiolarians (Fig. 11A) and

Table 4. Mean correlation coefficients of major and trace elements of black shale beds. The stratigraphically corresponding zones of the carbonate body are indicated for comparison

Beds	Zone	Al : Cr	Al : Mo	Al : Ni	Al : Zn	Al : Cu	Al : V	Al : Cd	Al : Co	Al : Re	Al : U	Cr : Cu	Mo : Ni	Mo : Zn	Mo : V	Ni : Zn	Zn : V	Zn : Cd
14	Cover bed	0.95	0.85	0.99	0.99	0.51	0.99	0.99	0.99	-0.62	0.80	0.76	0.90	0.91	0.75	1.00	0.96	0.97
13	4	0.35	-0.25	-0.25	0.01	-0.06	0.27	-0.67	0.95	0.29	-0.58	0.77	0.94	0.70	0.75	0.86	0.74	0.38
10 to 12	3	0.98	0.84	0.85	0.74	0.89	0.79	0.79	0.96	0.73	0.91	0.94	0.99	0.97	0.99	0.97	0.99	0.93
9	2	0.91	0.93	-0.18	0.44	0.41	0.93	0.41	0.99	-1.00	-0.98	0.00	0.20	0.74	1.00	0.81	0.73	1.00
6 to 8	1	0.27	0.39	0.24	0.24	0.29	0.26	0.37	0.92	0.19	0.10	0.98	0.97	0.96	0.95	0.97	0.89	0.96

clay minerals. Peloidal micrite is particularly abundant in zones 3 and 4, where it accounts for around 70% of the rock volume (Figs 10C and 11B). This micrite is characterized by abundant oval to spherically shaped peloids, which measure 100 to 500 μm in diameter. The peloids do not show any obvious internal structure and exhibit a cloudy and heterogeneous fabric. The space between the peloids is occupied by fine, dispersed equant calcite cement. Similar to the matrix micrite, the peloidal micrite exhibits scattered occurrences of *Palaxius* faecal pellets, gastropod, bivalve and ammonite shell fragments, as well as Foraminifera and radiolarian tests. The peloids and *Palaxius* faecal pellets are fluorescent under UV light, suggesting that they are enriched in organic matter compared to the surrounding micrite. *Palaxius* faecal pellets are present in all zones but are particularly common in zones 1 and 2 (Fig. 10B). The crescent-shaped canals are arranged in two groups around a symmetry plane, and are oriented in different directions towards and away from the symmetry plane. They are oval to spherical in shape and measure up to 500 μm in diameter. Their internal structure clearly distinguishes them from the aforementioned micritic peloids. Pyrite occurs as very small and finely dispersed grains measuring only several microns in size. In some rare cases pyrite also forms aggregates and clusters of idiomorphic crystals (Fig. 9B). Dolomite occurs within zones 1 and 2. The dolomite crystals are pale grey in colour and show well-defined crystal faces (Figs 9B and 10B).

The Amma Fatma limestone is penetrated by numerous veins, cracks and large cavities throughout zones 1 to 4. Cavities and veins show the same paragenetic mineral sequence in all zones: Matrix micrite or peloidal micrite represents the primary fabric of the rock. Cavities and veins are rimmed by microquartz, followed by equant calcite spar and megaquartz (Figs 10C, D, 11B, C, 12A and B). Microquartz (*sensu* Knauth, 1994) is pale brown to beige in colour (Figs 10C and 11B, C), and typified by very small grain sizes reaching no more than several microns in diameter. In places it can also be found finely dispersed among the equant calcite crystals. Microquartz occasionally forms crystal fans showing oscillatory extinction patterns under crossed polarized light. Volumetrically, equant calcite is the dominant void filling phase in all four zones (Figs 10A, 11C, 12A and B); its crystals measure up to 1 mm in diameter. The last phase in the paragenetic phase sequence is megaquartz (*sensu* Knauth, 1994). Megaquartz crystals reach up to 1 mm or more in diameter (Fig. 10C and D). An accessory peculiar carbonate phase present within fractures and voids is an authigenic rim of microcrystalline calcite referred to as seam micrite (Fig. 12). It is present in all zones and occurs exclusively along the outer rims of veins and cavities,

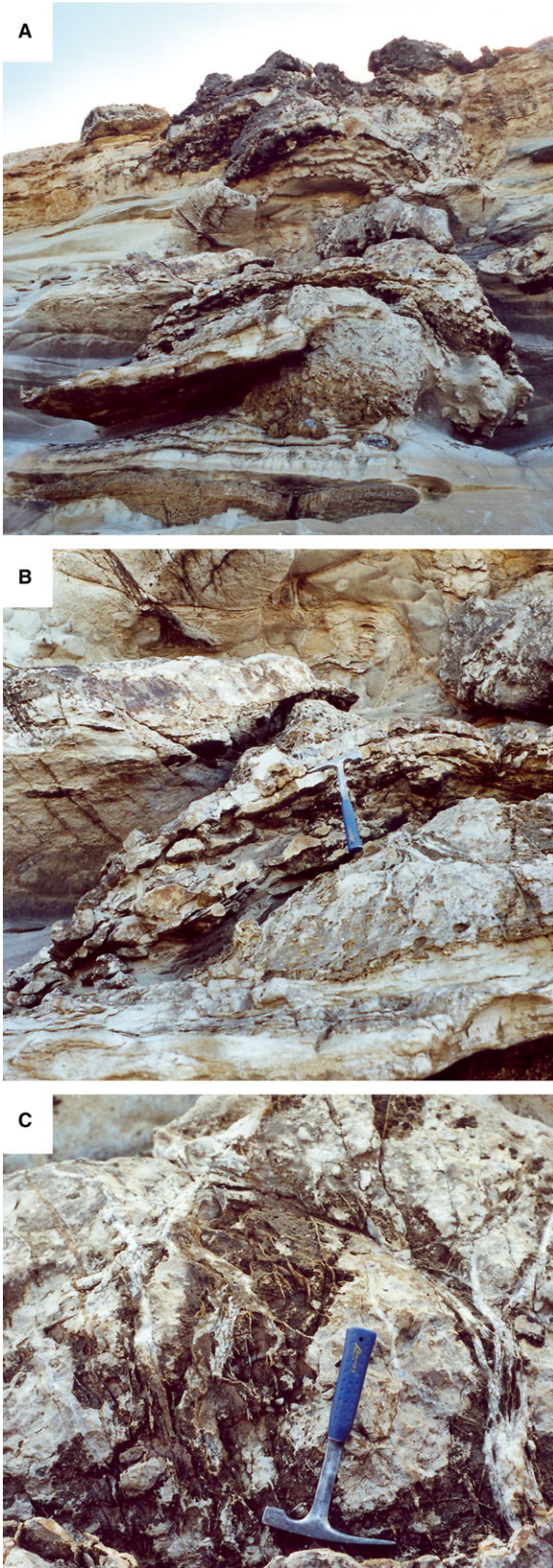


Fig. 7. (A) Bottom view of the Amma Fatma body. The width of the image is 4 m at the base of the carbonate body. (B) A carbonate bank separating zone 2 from zone 1, hammer for scale. (C) Concretionary carbonate from zone 2 penetrated by numerous carbonate veins, hammer for scale.

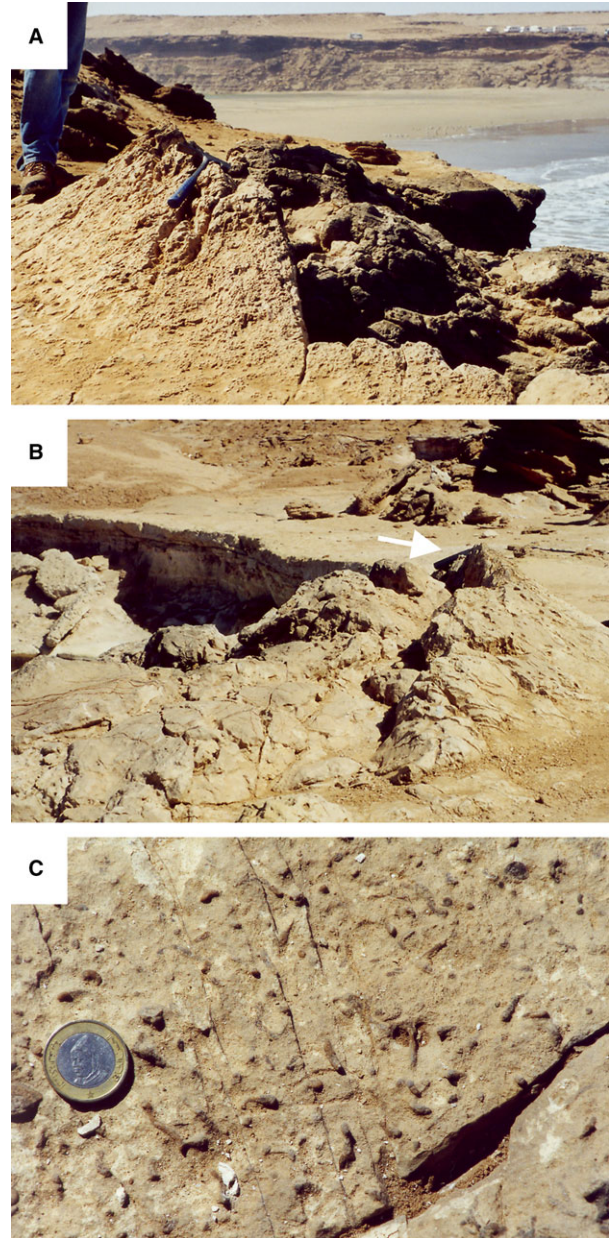


Fig. 8. Photographs from the topmost part of the body. (A) View from northeast, the cover bed capping the body bends upwards, hammer for scale (cf. Fig. 4A). (B) Same as (A), view from south-west, hammer (arrow) for scale. (C) Tubular fossils from zone 4 of the carbonate body, coin for scale.

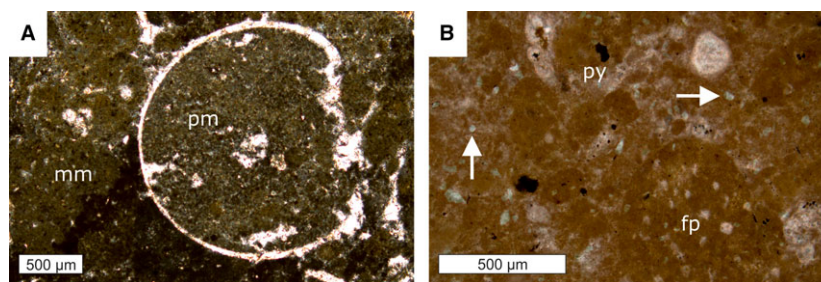


Fig. 9. Photomicrographs of zone 1 limestones; plane-polarized light. (A) Detritus-rich matrix micrite (mm) surrounding a gastropod shell filled by peloidal micrite (pm). (B) Stained thin section showing peloidal micrite with faecal pellets (fp), pyrite aggregates (py) and grey, unstained dolomite crystals (arrows).

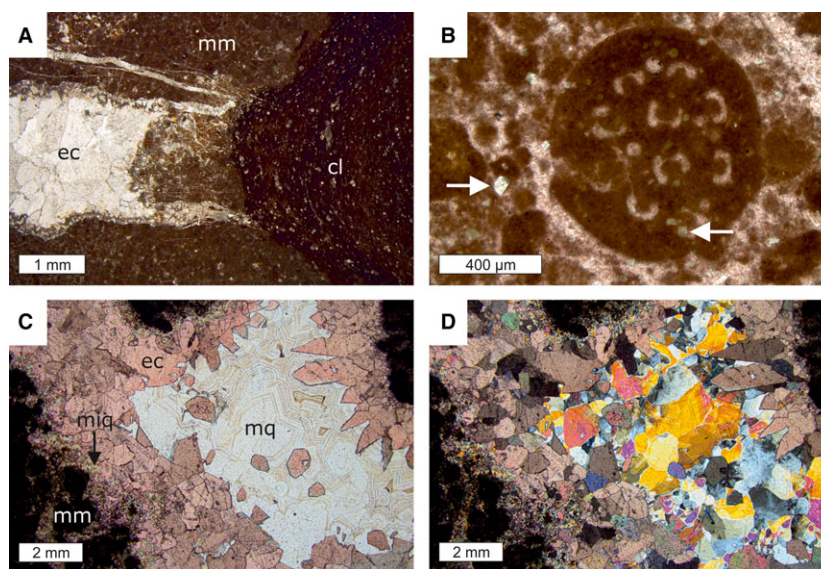


Fig. 10. Photomicrographs of zone 2 limestones. (A) Matrix micrite (mm) surrounding a large cavity filled by equant calcite (ec), several mm thick clay layers (cl) to the left; plane-polarized light. (B) Detailed view of a *Palaxius* faecal pellet with rhombohedral dolomite crystals (arrows); stained thin section, plane-polarized light. (C) Large cavity surrounded by matrix micrite (mm), rimmed by microquartz (miq) and equant calcite (ec); centre of the cavity is filled by large megaquartz crystals (mq); stained thin section, plane-polarized light. (D) Same photograph as (C) in crossed-polarized light.

where it forms highly irregular patches and fringes (Fig. 12A and B). Seam micrite is dark brown, almost black in colour and is very homogenous, showing no detrital inclusions. It shows strong epifluorescence when excited with UV light (Fig. 12C).

The carbonate cover bed (Fig. 4) shows a quite similar paragenetic phase sequence to zones 1 to 4 of the carbonate body (Fig. 4). The matrix comprises micrite, which, compared to the matrix micrite of zones 1 to 4, contains less detrital material. It is relatively homogeneous showing no clotted or peloidal textures and contains minor dolomite crystals (Fig. 13). The fossil content is low, represented by mainly radiolarian and foraminiferan tests (Fig. 13A). Similar to the carbonate body, the cover bed is penetrated by numerous cracks and veins, which have been filled by secondary precipitates. Cavities contain

microquartz and later formed equant calcite spar (Fig. 13B and C).

Macrofauna

The macrofossils collected from Zone 4 of the carbonate body comprise a low diversity molluscan assemblage of gastropods, bivalves and ammonites, together with *Palaxius* faecal pellets and burrows. The gastropods comprise 23 specimens of the aporrhaid *Drepanocheilus* sp. (Fig. 14A and B), mostly juveniles, but also a few adults up to 21 mm high, and a single, partially fragmented specimen that might represent a neogastropod belonging to the genera *Drilluta*, *Bellifusus* or *Paleopsephaea* (Fig. 14C). The bivalves belong to three taxa: a single articulated lucinid specimen (Fig. 14E), juvenile

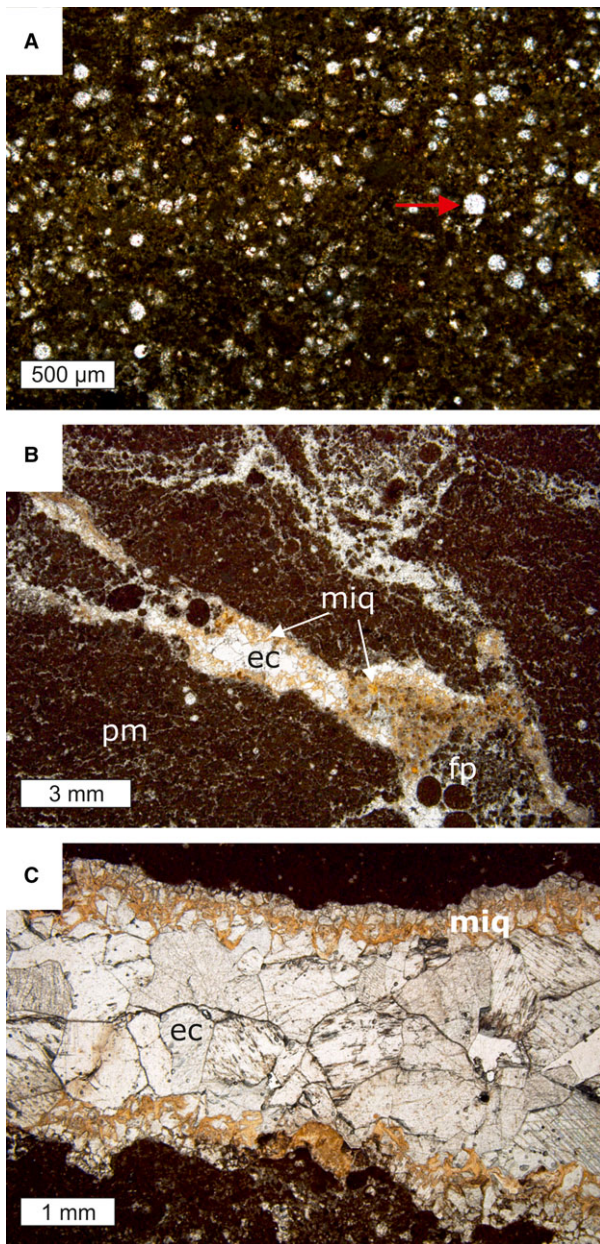


Fig. 11. Photomicrographs of zone 3 limestones; plane-polarized light. (A) Microcrystalline calcite matrix featuring abundant radiolarian tests (arrow). (B) Peloidal micrite with faecal pellets (fp) surrounding veins and cracks rimmed by microquartz (miq) and filled by equant calcite (ec). (C) Close-up view of a vein rimmed by microquartz (miq) and filled by equant calcite (ec).

inoceramids ($n = 4$; Fig. 14D) and gryphaeid oysters ($n = 6$), which could belong to the genus *Pycnodonte*. The small specimen sizes (<10 mm) of the two latter taxa and the articulation of the lucinid precludes further identification. The ammonites ($n = 5$) are juveniles and adults belonging to the genus *Benueites*, including *Benueites* cf. *benueensis*.

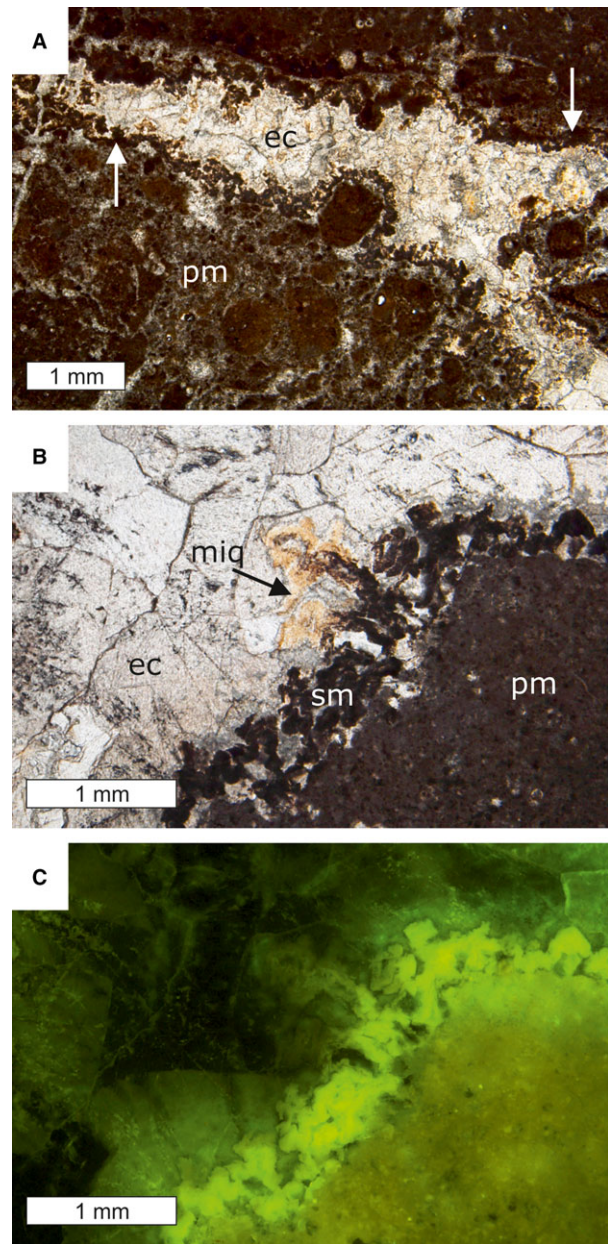


Fig. 12. Photomicrographs of zone 4 limestones. (A) Peloidal micrite (pm) surrounding a void filled by equant calcite (ec), arrows indicate seam micrite (sm) lining the cavity; plane-polarized light. (B) Close-up view of the seam micrite (sm), pm = peloidal micrite, miq = microquartz, ec = equant calcite; plane-polarized light. (C) Same detail as (B) under fluorescent light.

Isotope geochemistry, TC and TOC

Results of carbon and oxygen stable isotope analyses are shown in Fig. 15. Matrix micrite is ^{13}C -depleted to different degrees throughout all zones of the carbonate body, including the cover bed. It revealed the lowest $\delta^{13}\text{C}$ values

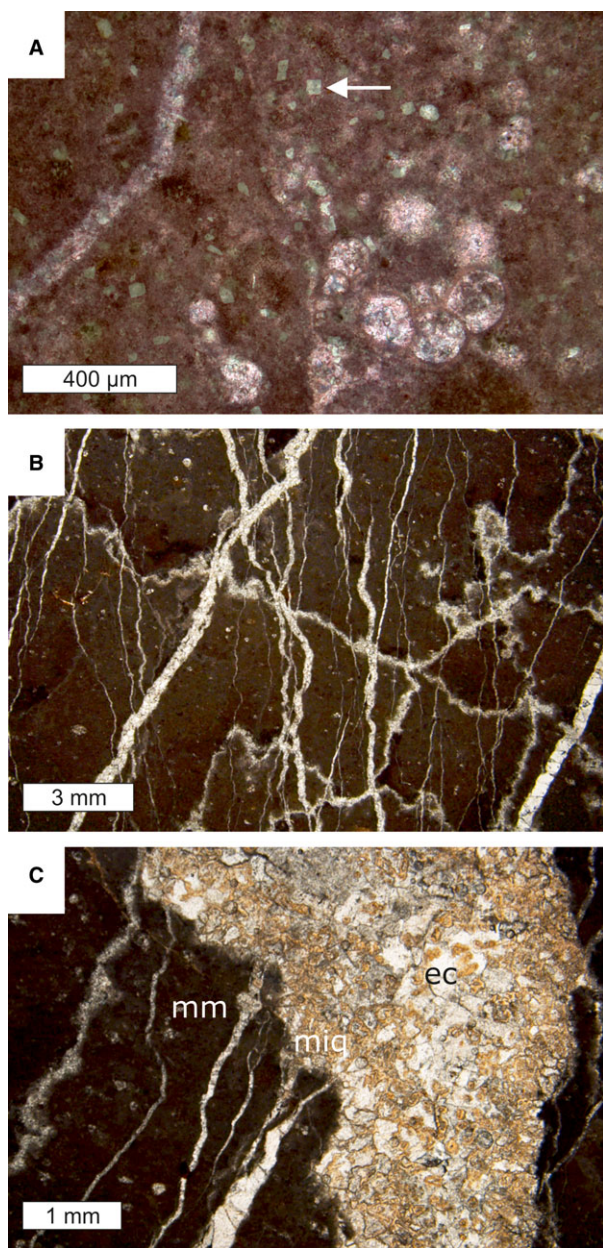


Fig. 13. Photomicrographs of the cover bed; plane-polarized light. (A) Close-up view of matrix micrite featuring dolomite crystals (arrow) and foraminifera tests, stained thin section. (B) Dark brown, fine-grained micrite pervaded by several veins made of secondary equant calcite. (C) Large cavity surrounded by matrix micrite (mm) and filled by microquartz (miq) and equant calcite (ec).

in zone 1, ranging from -23.5 to -21.3‰ . Zone 2 micrite yielded a wider range of values from -23.1 to -7.9‰ , and zone 3 micrite more positive values between -11.0 to -0.3‰ . Zone 4 micrite shows the largest scatter of $\delta^{13}\text{C}$ values, falling between -22.9 and -1.3‰ . The matrix micrite of the cover bed yielded $\delta^{13}\text{C}$ values from

-2.3 to -0.4‰ . The $\delta^{13}\text{C}$ values of equant calcite were analysed from zones 3, 4 and the cover bed. Generally, equant calcite is less ^{13}C -depleted than matrix micrite. A sample from zone 3 revealed the only positive $\delta^{13}\text{C}$ value of 1.6‰ . Samples from zone 4 and the cover bed show little heterogeneity and fall between -3.7 to -1.5‰ and -0.9 to -0.7‰ , respectively.

The $\delta^{18}\text{O}$ values of matrix micrite and equant calcite from all sections of the carbonate body are exclusively negative. Matrix micrites from zones 1, 2 and 3 exhibit values from -2.9 to -2.3‰ , -3.2 to -2.1‰ and -3.4 to -1.8‰ , respectively. Zone 4 matrix micrite displays more scattered $\delta^{18}\text{O}$ values from -4.3 to -1.7‰ . Matrix micrite of the cover bed yielded values from -3.3 to -2.6‰ . The $\delta^{18}\text{O}$ value of equant calcite from zone 3 and 2 is -3.4‰ . Equant calcite from zone 4 shows the most negative $\delta^{18}\text{O}$ values from -6.2 to -2.6 . Equant calcite of the cover bed is less ^{18}O depleted (-2.3 and -1.7‰).

A total of six samples from the Amma Fatma carbonate body were analysed for their TC and TOC contents (Table 5). The TOC content increases significantly from top to bottom, from 0.1% in zone 4 to 0.7% in zone 1. The cover bed exhibits a similar TOC content as the top-most zone 4 of 0.1% .

Biomarkers

Hydrocarbons

Organic matter enclosed in the sediments of the Tarfaya Basin has been shown to be of low maturity (Kolonic *et al.*, 2002; Sachse *et al.*, 2012). The hydrocarbon fraction before decalcification from the cover bed is characterized by short and long chain *n*-alkanes that range from C_{16} to C_{34} . The shorter-chain C_{16} to C_{20} *n*-alkanes dominate over longer chain *n*-alkanes, whereby *n*-alkanes peak at *n*- C_{20} . Apart from *n*-alkanes, the only compounds detected are minor amounts of the regular isoprenoids pristane and phytane, with phytane more abundant than pristane. The hydrocarbon fraction after decalcification from the cover bed shows a very similar pattern, except that the contents are much reduced compared to the fraction before decalcification.

Hydrocarbons in the extract before decalcification from zone 1 are characterized by the dominance of *n*-alkanes from C_{16} to C_{30} . In contrast with the cover bed, C_{16} and C_{18} dominate over C_{20} . Pristane and phytane are the only non-alkane compounds detected in zone 1, with phytane slightly more abundant than pristane. The hydrocarbon fraction after decalcification is similar to the fraction before decalcification except that the overall intensities of all compounds are greatly reduced. Very similar results

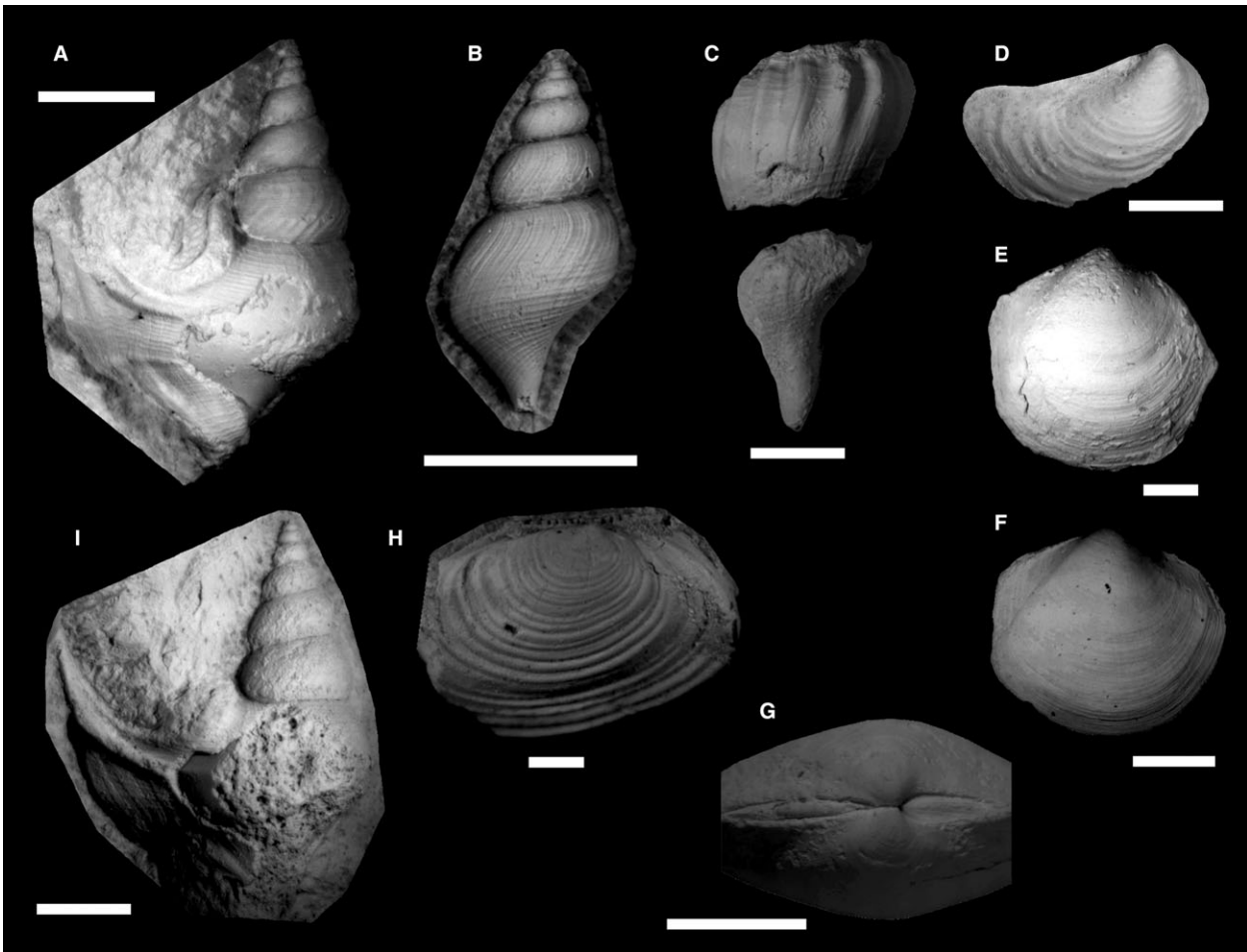


Fig. 14. Representative macrofossils from Amma Fatma Plage. Carbonate body: (A to E); bed 2 Amma Fatma section: (F to I) from collections of the Oxford University Museum, U.K. (KX codes). (A) Adult *Drepanocheilus* sp. (B) Juvenile *Drepanocheilus* sp. (C) Possible neogastropod; specimen at outcrop had siphon broken from (but still closely associated with) the main part of the body whorl. (D) Juvenile inoceramid. (E) Lucinid; right valve with partially fractured anterior margin. (F) Lucinid; right valve (KX.15683). (G) Lucinid; detail of dorsal margin of articulated specimen, anterior to right. Note well-developed lunule and calcified ligament (KX.15684). (H) Inoceramid, oblique dorsal view of right valve (KX.15696). (I) Adult *Drepanocheilus* sp. (KX.15683). All scales = 5 mm.

were obtained for two carbonate samples of zones 3 and 4, and are not further detailed here.

Carboxylic acids

Carboxylic acid fractions before and after decalcification from the cover bed and zone 1 limestone are shown in Fig. 16. The carboxylic acid fraction from the cover bed is dominated by saturated short chain *n*-fatty acids ranging from C_{12} to C_{18} . Most abundant *n*-fatty acids are C_{16} and C_{18} , which dominate over C_{12} . Unsaturated *n*-fatty acids and long-chained saturated *n*-fatty acids are present in very small amounts (Fig. 16A). The carboxylic acid fraction after decalcification varies only slightly from the fraction before decalcification, with medium-chain *n*-fatty

acids up to C_{23} more abundant in the former (Fig. 16B). The contents of short chained *n*-fatty acids are markedly decreased (ca 50% of all carboxylic acids) compared to the fraction before decalcification (Table 6), however, the distribution of C_{12} , C_{16} and C_{18} is similar.

The carboxylic acid fraction prior to decalcification of zone 1 limestone (Fig. 16C) is characterized by short-chained, C_{12} to C_{18} *n*-fatty acids. The C_{12} , C_{16} and C_{18} *n*-fatty acids are dominant over all other compounds. Additionally, $\alpha\beta$ - and $\beta\beta$ -hopanoic acids with 31 and 32 carbon atoms are accessory compounds. The carboxylic acid fraction after decalcification of zone 1 limestone (Fig. 16D) differs markedly from all other samples. Apart from short-chain *n*-fatty acids numerous middle- to long-chain compounds are abundant. These compounds

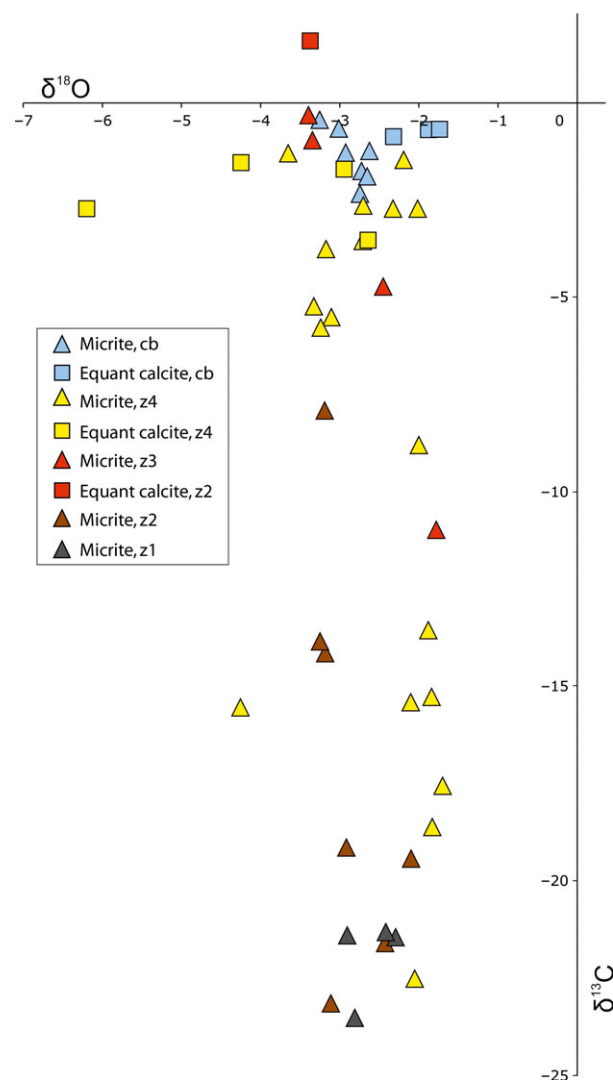


Fig. 15. Carbon and oxygen stable isotope cross-plot of carbonate phases from zones 1 to 4 (z1 to z4) and the cover bed (cb). All values are relative to V-PDB.

include C_{16} , C_{18} and C_{22} α,ω -diacids and minor hopanoic acids, namely C_{32} -17 β (H),21 β (H)-hopanoic acid. Acyclic to tricyclic biphytanic diacids were only found in zone 1 limestone. The mono- and bicyclic biphytanic diacids only contain cyclopentane rings, whereas the tricyclic biphytanic diacid contains two cyclopentane rings and one cyclohexane ring, according to its mass spectrum and retention time. Of all biphytanic diacids, bicyclic

Table 5. Total organic carbon (TOC) content of the zones of the carbonate body including the cover bed

Sample	Zone	TOC%	TIC%	TC%
M-01	Cover Bed	0.12	8.36	8.48
M-03	Zone 4	0.13	8.23	8.36
M-06		0.13	8.02	8.15
M-20	Zone 3	0.45	7.75	8.20
M-11	Zone 1	0.69	7.59	8.28
M-17		0.59	7.65	8.24

biphytanic diacid (BP-2) dominates over acyclic- (BP-0), monocyclic- (BP-1) and tricyclic- (BP-3) biphytanic diacids. BP-2 is strongly ^{13}C -depleted (-96‰), while BP-3 shows a higher $\delta^{13}C$ value of -22‰ .

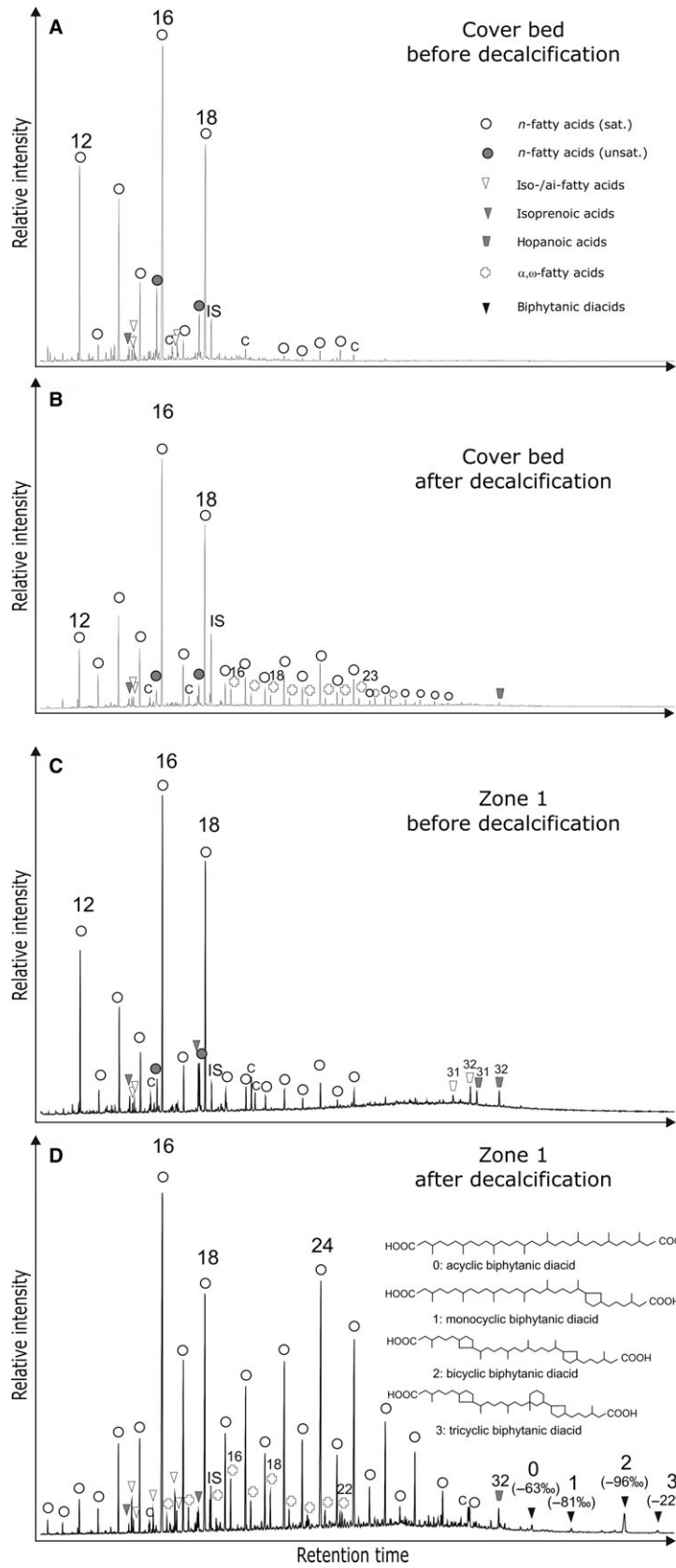
The total amount of carboxylic acids varies strongly between the samples. For the cover bed the amount of acids in the extract after decalcification is half that of the fraction before decalcification. For the samples from zones 4, 3 and 1 the ratio is reversed, where the carboxylic acids were found to be more tightly bound to the carbonate lattice. The amount of acids increases from zone 4 to zone 1. Contents and phase-specific stable carbon isotope values of the carboxylic acids are shown in Table 6.

INTERPRETATION AND DISCUSSION

The Amma Fatma carbonate body – A hydrocarbon seep deposit

The comprehensive data set obtained for the Amma Fatma carbonate body allows constraining of the geological setting and the processes that triggered its formation. Although this deposit is unlike many hydrocarbon-seep deposits in terms of its faunal content (cf. Campbell, 2006), there is multiple evidence that it formed at a shallow-water seep in a high productivity realm. The strongest indication for methane seepage is the presence of ^{13}C -depleted biphytanic diacids, which are molecular fossils of anaerobic methane oxidizing archaea (ANMEs; Birgel *et al.*, 2008a). These compounds are putative diagenetic breakdown products of glycerol dibiphytanyl glycerol tetraethers (GDGTs; Liu *et al.*, 2016) and are membrane lipids of archaea including ANMEs (see Schouten *et al.*, 2013 for a review). Biphytanic diacids with extreme ^{13}C -depletions have been reported from various methane-rich environments (Schouten *et al.*, 2003;

Fig. 16. Gas chromatograms (total ion currents) of the carboxylic acid fractions from total rock samples before decalcification (intercrystalline compounds) and from the residual powders after decalcification (intracrystalline compounds), IS = internal standard. (A) Carboxylic acids from the cover bed before decalcification. (B) Carboxylic acids from the cover bed after decalcification. (C) Carboxylic acids from zone 1 before decalcification. (D) Carboxylic acids from zone 1 after decalcification; numbers 0 to 3 refer to the biphytanic diacids BP-0 to BP-3, their $\delta^{13}C$ values are indicated in parentheses and are versus V-PDB.



Birgel *et al.*, 2008a; De Boever *et al.*, 2009; Natalicchio *et al.*, 2012). GDGTs and biphytanic diacids are uncommon in Mesozoic and Palaeozoic seep limestones, and the more persistent irregular isoprenoids crocetane and pentamethylcosane (PMI) have been used to track methane oxidation in the rock record (Birgel *et al.*, 2008b), but neither of these were found in the Amma Fatma deposit. The most abundant biphytanic diacid in the Amma Fatma limestone is BP-2. Values as low as -96‰ for BP-2 in the Amma Fatma deposit have only been reported from seep-dwelling ANMEs. A similar predominance of ^{13}C -depleted BP-2 among the biphytanic diacids was also reported for other Cenozoic and modern methane-seep carbonates (Birgel *et al.*, 2008a). In contrast with BP-2, BP-3 is derived from other sources, as indicated by its $\delta^{13}\text{C}$ value similar to that of crenarchaeol-derived tricyclic biphytanes of planktonic Thaumarchaeota (Könneke *et al.*, 2012; Schouten *et al.*, 2013; Pearson *et al.*, 2016).

Interestingly, biphytanic diacids are only present in the lowermost zone 1, suggesting a heterogeneous composition of the Amma Fatma carbonate body. In zones 2 to 4, however, biphytanic diacids and other molecular fossils of hydrocarbon seepage such as isoprenoid hydrocarbons are possibly obscured by hydrocarbons and unresolvable complex mixtures, similar to some modern seep carbonates, particularly oil-seep carbonates (Naehr *et al.*, 2009; Feng *et al.*, 2014). Since biphytanic diacids were only detected within the carboxylic acids fraction after decalcification, these compounds are tightly bound to the carbonate lattice and consequently reflect environmental conditions during authigenesis, consistent with anaerobic methanotrophy contributing to carbonate formation.

Many ancient seep limestones are typified by a distinct paragenetic sequence of mineral phases that enables the reconstruction of processes that governed their formation (Beauchamp & Savard, 1992; Campbell *et al.*, 2002; Peckmann *et al.*, 2002; Hagemann *et al.*, 2013; Zwicker *et al.*, 2015). Microcrystalline calcite (i.e. micrite) forms the matrix of most seep limestones, and several types can be distinguished including clotted (Peckmann *et al.*, 2002), peloidal (Roberts & Aharon, 1994) and detritus-rich matrix micrite (Kiel *et al.*, 2013; Tong *et al.*, 2016). Micrite of the Amma Fatma deposit exhibit a wide range of $\delta^{13}\text{C}$ values, a pattern commonly found for seep limestones (cf. Greinert *et al.*, 2001). The composition of the carbon pool from which carbonates precipitate at seeps varies over time and depends on the degree of mixing between various carbon sources (Suess & Whiticar, 1989; Peckmann & Thiel, 2004). Biogenic and thermogenic methane, higher hydrocarbon compounds including crude oil and dissolved inorganic carbon from sea water all contribute to the carbon pool of the parent fluid, and determining the contribution of each source to carbonate

precipitation at ancient seeps thus remains problematic. Sulphate-dependent AOM is considered to be the main process triggering carbonate precipitation at seeps, whereby the carbonates inherit the ^{13}C -depletion of the organic carbon sources (Ritger *et al.*, 1987; Peckmann & Thiel, 2004; Campbell, 2006). Regardless of the carbon source controlling the isotopic composition of the carbon pool, the carbonates that precipitate at seeps are usually more ^{13}C -enriched than the organic carbon sources due to an admixture of marine carbonate (Peckmann & Thiel, 2004).

The lowest $\delta^{13}\text{C}$ value of the Amma Fatma matrix micrite of -23.5‰ therefore suggests that AOM did not necessarily contribute substantially to carbonate precipitation, although ^{13}C -depleted biphytanic diacids testify to the presence of microbial communities performing AOM. Slightly lower $\delta^{13}\text{C}$ values were obtained from seep deposits associated with Jurassic black shales from Kilve, UK, and were attributed to biogenic methane production in the host sediments and its oxidation close to the sea floor (Xu *et al.*, 2016). The oxidation of higher hydrocarbon compounds may have contributed to carbonate formation at Amma Fatma. This notion, however, is rather speculative as evidence for the presence of oil at the ancient seep is missing, and it is only supported by $\delta^{13}\text{C}$ values that are within the range of carbonates precipitating at modern oil seeps (cf. Anderson *et al.*, 1983; Sassen *et al.*, 1999; Formolo *et al.*, 2004). A new approach using trace and rare earth metal contents may shed light on the composition of fluids of the Amma Fatma seep (cf. Smrzka *et al.*, 2016), and future work may assess the impact of crude oil at ancient seeps with more confidence. Finally, the Amma Fatma black shales themselves might have acted as a readily available source of organic carbon, causing microbially remineralization-driven carbonate formation. The $\delta^{13}\text{C}_{\text{TOC}}$ values of the Amma Fatma succession are slightly lower than the $\delta^{13}\text{C}$ values of the authigenic carbonates. Remineralization of large amounts of organic carbon buried during OAE 2 may have consequently contributed to carbonate precipitation, but it does not explain the presence of ^{13}C -depleted biphytanic diacids.

Seam micrite is a peculiar carbonate phase of the Amma Fatma deposit. Peckmann *et al.* (2003) described a similar phase in Eocene seep deposits from Washington State that also lines cavity walls and predates later-stage calcite cements. The purity and microfabric of the Amma Fatma seam micrite are indicative of an *in situ* precipitation, and its intense epifluorescence (Fig. 12C) distinguishes it from matrix and peloidal micrite. The latter observation suggests an increased content of organic residue, agreeing with an involvement of microbial activity in its formation (cf. Peckmann & Thiel, 2004). Equant

Table 6. Contents and compound-specific stable carbon isotope values of carboxylic acids. Summed up values are in ng g^{-1} rock, grouped lipid contents are in relative percentages of all carboxylic acids, $\delta^{13}\text{C}$ values in parentheses are in ‰ relative to V-PDB

Sample	Cover Bed		Zone 4		Zone 3		Zone 1	
	Before	After	Before	After	Before	After	Before	After
Short-chain <i>n</i> -fatty acids (14 to 18)	87% (-30‰)	58% (-30‰)	88% (-30‰)	58% (-31‰)	76% (-31‰)	28% (-30‰)	68% (-30‰)	35% (-30‰)
Long-chain <i>n</i> -fatty acids (26 to 32)	0	4% (n.m.)	2% (n.m.)	9% (-31‰)	1% (n.m.)	31% (-31‰)	1% (n.m.)	17% (-31‰)
Iso- & anteiso-fatty acids (15 and 17)	5% (n.m.)	2% (n.m.)	0	1% (n.m.)	0	0	2% (n.m.)	3% (n.m.)
Short-chain α,ω -diacids (14 to 24)	0	4% (n.m.)	0	3% (n.m.)	0	0	0	5% (n.m.)
Long-chain α,ω -diacids (25 to 28)	0	3% (n.m.)	0	3% (n.m.)	0	0	0	0
Hopanoic acids ($\alpha\beta$ 31/32 and $\beta\beta$ 31/32)	0	<1% (n.m.)	0	2% (n.m.)	5% (-32‰)	0	6% (-31‰)	1% (n.m.)
Biphytanic diacids (BP 0 to 3)	0	0	0	0	0	0	0	3% (-66‰)
Others	8%	29%	10%	25%	18%	40%	23%	36%
Sum of all carboxylic acids [ng g^{-1} rock]	2322.2	1117.3	2235.4	4640.5	3149.1	4886.9	3191.8	5925.5

calcite is a typical, later-stage mineral phase of seeps limestones (Campbell *et al.*, 2002; Peckmann *et al.*, 2003), and is interpreted as an abiotically formed cement that precipitated during increasing burial and progressive diagenesis, which agrees with the only moderate ^{13}C -depletion of the Amma Fatma equant calcite.

Authigenic silica minerals typify many Mesozoic and Cenozoic seep limestones (Goedert *et al.*, 2000; Himmler *et al.*, 2008; Peckmann *et al.*, 2011; Kuechler *et al.*, 2012; Kiel *et al.*, 2013; Smrzka *et al.*, 2015). Most of the dissolved silica required for quartz precipitation in seep and non-seep environments is derived from the dissolution of radiolarian tests, diatom frustules and sponge spicules (Lancelot, 1973; Von Rad *et al.*, 1977; Bohrmann *et al.*, 1994; DeMaster, 2002; Kuechler *et al.*, 2012), although dissolution of volcanic glass and clay minerals may also become relevant during late burial diagenesis (Keene, 1975). The abundance of radiolarian tests within the Amma Fatma carbonate body (Fig. 11A) suggests a biogenic source of silica. The sequence of microquartz occurring as thin linings along crack and cavity walls (Figs 11B, C and 12) and later megaquartz occluding large cavities (Fig. 10C and D) is typical of seep limestones (Smrzka *et al.*, 2015). The presence of silica polymorphs suggests that changing silicic acid concentrations controlled the mineralogy of the precipitate over time (Heany, 1993), whereby microquartz precipitated from fluids with higher concentrations of silicic acid and megaquartz formed during a later stage when silica concentrations had decreased.

Although the Amma Fatma deposit features mineral phases that are common in ancient and modern seep limestones, it lacks a carbonate phase that typifies many seep deposits, namely banded and botryoidal aggregates of fibrous aragonite cement. This type of cement typically exhibits low $\delta^{13}\text{C}$ values, reflecting its origin from AOM (Beauchamp & Savard, 1992; Roberts *et al.*, 1993; Savard *et al.*, 1996). The lack of this phase together with the dominance of micrite suggests that the Amma Fatma seep was characterized by diffusive rather than advective seepage of hydrocarbon-rich fluids (cf. Peckmann *et al.*, 2009).

Benthonic fauna

The benthonic macrofossil assemblage of the top part of the Amma Fatma carbonate body includes aporrhaid (*Drepanocheilus* sp.) and possible neogastropod gastropods, lucinid, inoceramid and gryphaeid (*Pycnodonte* sp.) bivalves. The small inoceramids and gryphaeids were epifaunal filter feeders, and the lucinid was an infaunal taxon that almost certainly had sulphide-oxidizing chemosymbionts, by comparison with modern members

of this family (Dando *et al.*, 1986). The aporrhaid was an epifaunal/shallow infaunal suspension or deposit feeder. The possible neogastropod was most likely epifaunal, but without further taxonomic information its diet cannot be inferred. The presence of this fauna suggests that oxygenated conditions were at least episodically present in the water column and sediment during the formation of at least the upper part of the carbonate body, although the absence of large inoceramid and oyster specimens may hint at challenging environmental conditions. A taxonomically very similar low diversity fauna is present in shell-rich micritic carbonate concretions from below the carbonate body in bed 2 at Amma Fatma Plage, collected by Andrew Gale in 2003 and now housed in the collections of the Oxford University Museum, UK. This includes the same species of lucinid (Fig. 14F and G) and *Drepanocheilus* sp. (Fig. 14I), but also much larger inoceramids (up to 35 mm long, Fig. 14H). Furthermore, species of *Pycnodonte*, inoceramids, lucinids and aporrhaid gastropods are common elements in Late Cretaceous faunas from across North Africa (Busson *et al.*, 1999; El Qot, 2006; Ayoub-Hannaa *et al.*, 2014). This indicates that the Amma Fatma seep fauna contains mostly elements of normal marine background faunas, and lacks specialized obligate taxa, possibly apart from the lucinid, which might belong to the seep obligate genus *Nymphalucina* (Kiel, 2013), although is also similar to the lucinid figured in El Qot (2006, plate 14, figs 7 to 10) as *Lucina fallax* Forbes, 1846 from the Late Cenomanian of Egypt. This paucity of obligate seep taxa is a common feature of shallow water seep faunas in the Mesozoic and Cenozoic (Kiel, 2010; Little *et al.*, 2015). Other examples include the slightly older Cenomanian Tropic Shale seep faunas from southern Utah, USA (Kiel *et al.*, 2012), which are dominated by mostly small specimens of the bivalve genera *Inoceramus* and *Nymphalucina*, the gastropod genus *Drepanochilus*, rarer examples of the neogastropod *Paleopsephaea* and *Callianassa* decapod claws. A younger example is the Paleocene Panoche Hills seep deposit from California, USA (Schwartz *et al.*, 2003), which contains numerous specimens of *Nymphalucina* and less common aporrhaid gastropods (Kiel, 2013).

The *Palaxius* faecal pellets found throughout the Amma Fatma carbonate body are microcoprolites, which are today produced by callianassid decapod crustaceans. *Palaxius* microcoprolites are common in Palaeozoic and Mesozoic shallow water limestones (Senowbari-Daryan *et al.*, 1992; Schweigert *et al.*, 1997) and other methane-seep deposits (Peckmann *et al.*, 2007; Senowbari-Daryan *et al.*, 2007; Zwicker *et al.*, 2015). The number and shape of the crescent shaped canals in the Amma Fatma microcoprolites strongly resemble *Palaxius decemlunulatus*, which has previously been found in Cretaceous shallow

water carbonate deposits of northern Africa (Senowbari-Daryan & Kuss, 1992). The high density of *Palaxius* microcoprolites in the Amma Fatma body suggests high productivity and organic matter availability, sustaining dense populations of crustaceans.

Mode of formation of the Amma Fatma carbonate deposit

The Amma Fatma carbonate body is not older than Lower Turonian in age. The presence of ammonites belonging to the genus *Benueites* in zone 4 shows that the upper part of the seep deposit belongs to the *nodosoides* Zone, the youngest zone of the Lower Turonian, as elsewhere in the Tarfaya Basin. *Benueites* species, including *benueensis*, are associated with *Mammmites nodosoides* (Collignon, 1966). El Albani *et al.* (2001) described the laminated marls at Amma Fatma and deduced an early Turonian age based on the ammonite fauna and planktonic Foraminifera. The macrofaunal assemblage of the upper part of the Amma Fatma deposit suggests that the entire water column was at least episodically oxygenated at that time. The absence of the diagnostic $\delta^{13}\text{C}$ isotope excursion observed for OAEs confirms that the black shales and the carbonate body formed in the aftermath of OAE 2, and is consistent with biostratigraphic evidence.

The Amma Fatma deposit is a tall, concretionary carbonate body, and in this respect resembles some of the exhumed Oxfordian seep deposits from Beauvoisin (Peckmann *et al.*, 1999) and Miocene deposits of Italy (Conti *et al.*, 2004). Concretions of various shapes and sizes are common in Mesozoic strata, and typically stand out from the host sediment after erosion (Coleman, 1993; Coleman & Raiswell, 1995; Sellés-Martínez, 1996; Seilacher, 2001; Marshall & Pirrie, 2013; Liang *et al.*, 2016). What is most indicative of concretionary growth is that the Amma Fatma carbonate body clearly stands out from the host successions. Apart from this large carbonate deposit, laminated strata from Amma Fatma and Mohammed Plage feature isolated, nodular, diagenetic concretions that precipitated within the organic carbon-rich limestones and black shales (El Albani *et al.*, 1997, 1999a). El Albani *et al.* (2001) described lower Turonian, elongated carbonate concretions in direct proximity to the Amma Fatma carbonate body. These concretions formed during early diagenesis before significant compaction occurred, as fossils were well-preserved and surrounding beds of the host marls wrap above and below the outside of the concretions. The Amma Fatma deposit crosses almost the entire section of laminated shales and limestones, making it difficult to ascertain if the carbonates precipitated during or after their deposition.

The cover bed capping the Amma Fatma deposit sheds light on the mode of accretion. It thins out around the top of the carbonate body (Fig. 8A and B), which agrees with the presence of a relief on the sea floor during the time of deposition. Such a scenario is in contrast with a thickening of a cover bed as seen during pockmark formation (cf. Agirrezabala *et al.*, 2013). The circumstance that the cover bed is much thinner directly on top of the seep deposit, and thickens readily away from it, indicates that the deposit was elevated above the sea floor. Given the changing environmental conditions, the carbonate body may have projected into the water column during episodes of sulphidic bottom waters as observed today in the Black Sea (Peckmann *et al.*, 2001). However, there is no evidence for an ancient hardground or firmground, as cementing epifauna are absent. It is conceivable that concretionary growth accompanied by compaction of the host sediment were the main modes of accretion of the Amma Fatma carbonate body, and that carbonate precipitation occurred in the subsurface but close to the sea floor. Large concretionary bodies require a constant and large supply of pore water that transports the necessary solutes to the locus of precipitation (Raiswell & Fischer, 2004; Mozley & Davis, 2005). Diffusive and advective transport of solutes by seeping fluids is the most likely mechanism that sustained concretionary growth over long timescales that subsequently fostered compaction and cementation of the Turonian black shales and marly limestones.

Mean $\delta^{18}\text{O}$ values of the predominantly authigenic matrix micrite ranging between -2.6 and -2.9‰ also point towards precipitation close to the sea floor, as they are within the range of values for limestones that precipitated in equilibrium with Cretaceous sea water at Mohammed Plage (cf. Kuhnt *et al.*, 2009). They show no appreciable deviation throughout the body, suggesting that pore waters did not experience large temperature shifts or meteoric water input that would have produced more negative $\delta^{18}\text{O}$ values (Hudson, 1978; Astin & Scotchman, 1988). Such fairly homogeneous oxygen isotope compositions are common for concretions that grew in shallow sediments close to the sea floor (Hudson & Friedman, 1974; Raiswell & Fisher, 2000). The $\delta^{18}\text{O}$ values of the later-stage equant calcite do not differ substantially from those of the matrix micrite, suggesting that neither phase experienced much elevated temperatures during burial diagenesis (cf. Campbell *et al.*, 2002).

In contrast, the trend towards lower $\delta^{13}\text{C}$ values from the topmost zone 4 to the lowermost zone 1 (Fig. 15) is interesting. The bottom zone 1 not only shows the highest ^{13}C depletion, but also the sole occurrence of biphytanic diacids and the highest TOC content. Explaining these patterns is challenging, as the preferential growth

direction of the Amma Fatma deposit is not obvious. Neither pervasive growth, outward, downward, nor upward growth can be excluded, and assumptions on the mode of accretion remain speculative. Seep carbonate formation is fuelled by a source of reduced, hydrocarbon-rich fluids from below. Zone 1 was possibly affected most by these fluids, which drove microbial activity as evidenced by the occurrence of ^{13}C -depleted biphytanic diacids. Fluid seepage apparently continued during ongoing sedimentation of organic material, and zone 1 remained the hotspot of hydrocarbon-driven authigenesis that clogged up the pore space and reduced permeability. The impact of methane-bearing fluids on carbonate precipitation in the upper zones 3 and 4 was apparently lower, resulting in gradually less negative $\delta^{13}\text{C}_{\text{carbonate}}$ values as the dominant carbon source changed from isotopically lighter, seepage-derived hydrocarbons to heavier organic matter derived from the host black shales associated with OAE 2.

Methane seepage and carbonate precipitation in the aftermath of OAE 2

The depositional environment of Amma Fatma Plage was most likely an outer shelf setting, as suggested by the foraminiferal assemblages and smectite-dominated clay mineral assemblages (Holbourn *et al.*, 1999) as well as the macrofossil content of the seep deposit (see above). The three palaeoecologically significant Foraminifera species identified at Amma Fatma are *Zygodiscus* (= *Zeugrhabdotus*) *erectus*, *Rhagodiscus splendens* and *Eprolithus floralis*. Generally, temperature and trophic resources are considered the most important factors affecting the distribution of calcareous nannoplankton, whereby ecological preferences of some species are already partly known (Eshet & Almogi-Labin, 1996; Mattioli, 1997; Lüning *et al.*, 1998; Herrle, 2003). The foraminiferal assemblages in combination with the occurrence of radiolarians and diatoms suggest high surface water productivity (El Albani *et al.*, 1999b; Holbourn *et al.*, 1999). Specifically, *Zygodiscus* (= *Zeugrhabdotus*) *erectus* is interpreted as an indicator for high productivity (Roth, 1981; Roth & Krumbach, 1986; Erba *et al.*, 1992; Herrle, 2003). This species is abundant throughout the Amma Fatma section and lacks any systematic distributional changes, suggesting persistent high productivity conditions throughout the entire section consistent with overall high carbon burial. Another species identified as high productivity-prone is *Rhagodiscus splendens*. This may indicate further intensification of upwelling conditions, possibly marking high productivity phases at the base and the top of the section within a generally highly productive setting. An additional argument for upwelling conditions is the presence of

Eprolithus floralis, which is also considered to be an indicator for cooler waters (Kuhnt *et al.*, 2001). The co-occurrence of these three species suggests that intensified upwelling of relatively cool, intermediate water occurred during the lower Turonian along the Tarfaya shelf. This interpretation is supported by pronounced peaks in phosphorus content that coincide with higher abundances of *Eprolithus floralis* and *Rhagodiscus splendens* at the bottom and top parts of the Amma Fatma section (Fig. 5). These observations, together with the characterization of the macrofaunal assemblage, help to reconstruct the environmental conditions in which the Amma Fatma seep deposit formed.

Carbonates from zone 4 and the cover bed formed under the influence of more prolonged periods of oxygenated conditions. The occurrence of marine background fauna suggests that it dominated and out-competed any specialized seep-specific taxa in this shallow water and high productivity environment. The absence of benthonic macrofauna in the lower part of the body might suggest lower levels of oxygen compared to the upper part. The presence of *Palaxius* in the lower part does not contradict this notion, as callianassid decapod crustaceans can tolerate extended periods of anoxia (Forster & Graf, 1992; Anderson *et al.*, 1994; Bromley, 1996). The carbonate body formed either during or shortly after deposition of the host strata, and vital information on the environmental conditions can be derived by analysing the trace metal content of host black shales and limestones. Organic-rich shales are distinctly enriched in trace metals including Cr, Mo, U, Ni, Zn, Cu, V, Cd, Co and Re, whereby the modes and mechanisms of enrichment differ somewhat between these elements (Calvert & Pedersen, 1993; Algeo & Maynard, 2004; Brumsack, 2006). The fact that all trace metals – with the exception of Cr and Co – do not correlate with Al confirms that their authigenic enrichment is due to geochemical changes in bottom and pore waters. The use of Cr in palaeoenvironmental analysis has been cautioned, as it is to a large degree of detrital provenance and is highly mobile in marine sediments (Tribovillard *et al.*, 2006). Cobalt mainly resides within the aluminosilicate fraction of the black shales as it shows the strongest correlation with Al of all trace metals, and will be consequently omitted from the discussion below. Black shale beds 7 to 13 show EFs of varying magnitudes, which argue for changing environmental conditions during deposition (Table 3). Molybdenum, Cd, Re and U exhibit the highest EFs. Molybdenum behaviour in sedimentary pore waters is linked to the presence of hydrogen sulphide that causes a speciation change from oxidized Mo to reduced thiomolybdate, which can be much more readily deposited either on organic species, or be incorporated and co-precipitated by iron sulphides (Helz *et al.*,

1996). Cadmium exhibits a similar behaviour towards dissolved hydrogen sulphide, except that it accumulates as a separate sulphide phase and can be just as easily enriched in barely reducing conditions at very low hydrogen sulphide concentrations (Rosenthal *et al.*, 1995). The ease of Cd enrichment in anoxic sediments and its high sensitivity towards hydrogen sulphide leads to high EFs, as well as to the large spread in EFs and total concentrations between zones 1 and 4 (Tables 2 and 3). Rhenium EFs are the highest on average of any trace metal. This is due to its very low crustal concentrations and the ease with which it accumulates in anoxic sediments (Crusius *et al.*, 1996). Rhenium enrichment does not require the presence of free hydrogen sulphide or Fe or Mn (oxy)hydroxides, and is solely controlled by the redox potential of the ambient water (Morford *et al.*, 2005). This suggests that the sediments in which carbonates of zones 1 to 4 formed were all characterized by a very shallow oxygen penetration depth or, more likely, periodically anoxic bottom waters.

In modern sediments U enrichment is observed at redox potentials present within the Fe reduction zone, before Mo accumulation occurs under more reducing conditions (Morford & Emerson, 1999). It has been argued that preferential U over Mo uptake is an indicator for suboxic conditions, whereas the reverse is the case when pore waters are strongly sulphidic (Algeo & Tribovillard, 2009). The decrease in Mo/U ratios, total Mo concentrations and Mo, Cd and Re EFs, combined with the concomitant increase in U content from zone 1 to 4 suggests a trend from euxinic conditions in zone 1 to more mildly anoxic conditions in zone 4. Nickel and Zn accumulate most effectively under euxinic conditions and reside in Ni- and Fe-sulphides, respectively (Algeo & Maynard, 2004). Vanadium can also accumulate efficiently within the nitrate reduction zone of marine sediments, and does not necessarily require dissolved sulphide. However, the combined enrichment of V, Zn, Ni and Mo suggest at least temporal euxinia at the sediment-water interface throughout zones 1 to 4 (cf. Hetzel *et al.*, 2009). The notion that ambient water mass chemistry lead to authigenic enrichment of Mo, Ni, Zn, V and Cd is supported by the strong positive correlation between these elements, and their lack of correlation to Al (Table 4).

Trace metal contents of black shales and limestones are governed by bottom water redox conditions, as well as sedimentary redox conditions. Redox-sensitive metals precipitate at redox boundaries in the sediments that often lie substantially below the sediment surface, which may lead to a strong offset between the age of authigenic precipitates and the age of the sediment in which the elements are enriched. It can therefore be difficult to

discriminate between enrichment of trace metals via direct precipitation from bottom waters, and enrichment via the precipitation of solid phases within redox zones in the sediment (cf. Kasten *et al.*, 2003; Reitz *et al.*, 2004). However, this age offset between authigenic minerals and the host sediment decreases the more the redox zonation is compressed in the sediment like in the case of anoxic bottom waters. Analyses of trace metal enrichment argue for a formation of black shale and marly limestone beds 7 to 14 under episodic euxinic bottom waters. More importantly, the distribution of Mo, U, Cd and Re implies changes in hydrogen sulphide content of the water mass, from higher contents in zone 1 to lower contents in zone 4. This questions the proposition that the carbonate body grew in its entirety and simultaneously within the shales and limestones. Zone 4 carbonates formed under at least episodically oxygenated conditions, which would have hampered the formation of black shales in bed 13.

Despite the occurrence of macrofossils in zone 4, the Amma Fatma body is poor in fossils compared to most Phanerozoic seep deposits, which are usually replete in shelly macrofauna (Campbell & Bottjer, 1995; Kiel & Peckmann, 2007; Little *et al.*, 2015). Most of the shells identified in thin sections are severely fragmented and were most likely transported to the site over some distance, indicating that most of these molluscs did not live at the seep. Environmental conditions for macrofaunal species at the Amma Fatma seep were at the very least challenging, if not precluding their survival altogether. Euxinic conditions occurred during all stages of carbonate precipitation, interrupted by sporadic oxygenation during formation of zone 4 that enabled macrofaunal assemblages to temporarily colonize the seep. Bottom water conditions were temporarily sulphidic, as were the shallow sediments where carbonate precipitation occurred, consistent with reconstructions for the wider Tarfaya palaeo-shelf area (Kolonik *et al.*, 2005; Poulton *et al.*, 2015). The carbonate mineralogy of the Amma Fatma seep deposits is almost exclusively calcite, lacking any banded and botryoidal aragonite cement. Calcite precipitation at seeps is favoured over aragonite precipitation under the influence of strongly reducing pore waters with low sulphate concentrations (Haas *et al.*, 2010; Nöthen & Kasten, 2011). The environmental conditions as constrained by trace metal analyses of the black shales did consequently not only govern the mode of accretion, but apparently influenced the mineralogy of authigenic carbonate at the Amma Fatma seep as well.

At passive continental margins various processes control the mechanism of fluid flow from sea floor sediments, including tectonic processes, thermohaline convection, sea-level changes and changes in

sedimentation rates (Judd & Hovland, 2007; Suess, 2014). Relevant factors that may have influenced the mode of seepage in the Cretaceous Tarfaya Basin include differential compaction and pore water overpressure, both of which are in turn controlled by sedimentation rates and changes in sea-level. Low sea levels promote seepage of fluids through the sediment column (Teichert *et al.*, 2003), as the hydraulic pressure needs to exceed the pressure of the water column to enable upward fluid flow towards the sea floor (Carson & Screaton, 1998). High-frequency sea-level changes at Amma Fatma Plage are indicated by intercalations of bioclastic storm beds into the marly, hemipelagic background sediments (cf. El Albani *et al.*, 1999b). The Amma Fatma coastal section is early Turonian in age, and studies from the Tarfaya Basin have demonstrated that the sea-level rose continuously during the Cenomanian due to a combination of eustatic sea-level rise and shelf subsidence (Gebhardt *et al.*, 2004; Mort *et al.*, 2008; Kuhnt *et al.*, 2009). This sea-level rise culminated during the earliest Turonian where sea-levels were possibly up to 250 m higher than today, the highest during the Cretaceous (Haq, 2014). However, Kuhnt *et al.* (2009) inferred that the lowermost Turonian at Mohammed Plage was characterized by a sea-level lowstand, linked to the ephemeral build-up of Antarctic ice sheets during that time. This is in accord with the inferred outer shelf water depths at Amma Fatma, which should have promoted seepage of hydrocarbon-rich fluids due to the comparatively low pressure of the water column. The presence of shallow water species *Broisonia enormis* and the abundance peak of *Gartnerago segmentatum* (Thierstein, 1976; Hattner *et al.*, 1980) further suggests that a short-term shallowing event may have occurred. Finally, El Albani *et al.* (1997) noted an upward increase in the frequency and thickness of the storm beds, and interpreted this observation as evidence for a falling sea-level through the section corresponding to the eustatic sea-level development during the late Early Turonian also suggested by Hardenbol *et al.* (1998).

Apart from sea-level changes, sedimentation rates also affect seepage dynamics in continental margin sediments. Sedimentation rates in the Tarfaya Basin during OAE 2 were estimated to have been above 10 cm kyr⁻¹ (Kuhnt *et al.*, 2005), or correspond to 4.8 cm kyr⁻¹ at well S13 (see Fig. 2) and 1.6 cm kyr⁻¹ at Mohammed Plage (Kolonik *et al.*, 2005). Despite the differences in these reconstructions, all estimates reflect high sedimentation rates. Such high sedimentation rates increase sediment loading on the continental slope that can lead to pore water overpressure, which squeezes reduced fluids from the underlying organic carbon-rich source rocks towards the sea floor (cf. Suess, 2014). Taken together, favourable conditions for seepage over long timescales were apparently favoured

by a relative sea-level fall and high sedimentation rates, which facilitated the precipitation of large amounts of authigenic carbonate at the Amma Fatma seep.

CONCLUSIONS

The Amma Fatma carbonate body is an unusual seep deposit, as seep-endemic macrofauna that characterizes many other seep deposits is absent. Nonetheless, lipid biomarkers testify to the presence of microbial communities that performed AOM and contributed to authigenic carbonate formation. With $\delta^{13}\text{C}$ values of matrix micrite as low as -23.5‰ it appears that anaerobic oxidation of methane was not the only trigger for carbonate precipitation. Remineralization of organic matter residing in the host black shales may have been an additional source of carbon for limestone formation. Persistent seepage was probably favoured by a sea-level lowstand and high sedimentation rates. The Amma Fatma deposit formed during the aftermath of OAE 2 over a considerable length of time. High productivity and partly euxinic conditions resulted in the deposition and preservation of black shales rich in organic matter. The Amma Fatma deposit is poor in macrofossils, and those present in the uppermost zone 4 are all Cretaceous shallow water species. Their presence testifies to the sporadic occurrence of oxygenated conditions in the bottom water. However, nannofossil distribution and pronounced enrichments of trace metals within the host strata point towards a high productivity setting with recurrent episodes of euxinia that shaped the shallow marine environment. Identifying seep deposits in such a shallow water setting poses a challenge. Diagnostic signals are masked by high primary production favouring heterotrophic taxa, which take advantage of the vast amounts of organic matter derived from photosynthetic primary production and outcompete obligate, endemic chemosymbiotic seep fauna. The Amma Fatma carbonate body may serve as an example on how to identify seep deposits in high productivity, shallow water settings. In such an environment, only a combination of methods will allow to ascertain that authigenic carbonate deposits formed at hydrocarbon seeps, and to constrain the modes of carbonate formation.

ACKNOWLEDGEMENTS

We thank Lukas Gerdenits for analytical support, Leopold Slawek for the preparation of thin sections, Susanne Gier for XRD measurements, Petra Körner for LECO measurements, Sabine Kasten and Matthias Zabel for help with element analysis and Sylvain Richoz for stable isotope analyses of carbonate samples. CTSL thanks Louella Saul, Annie D'Hondt, Franz Fürsich, Wagih Hannaa, Dick

Squires, Andrew Gale, Steffen Kiel and Jim Kennedy for advice about macrofossil identifications, and Eliza Howlett for access to specimens curated in the Oxford University Natural History Museum. Comments by Sabine Kasten and the two journal reviewers Nicolas Tribovillard and an anonymous referee are gratefully acknowledged.

References

- Agirrezabala, L.M., Kiel, S., Blumenberg, M., Schäfer, N. and Reitner, J.** (2013) Outcrop analogues of pockmarks and associated methane-seep carbonates: a case study from the Lower Cretaceous (Albian) of the Basque-Cantabrian Basin, western Pyrenees. *Palaeogeogr. Palaeoclimatol. Palaeoecol.*, **390**, 94–115.
- Algeo, T.J. and Maynard, J.B.** (2004) Trace-element behavior and redox facies in core shales of Upper Pennsylvanian Kansas-type cyclothems. *Chem. Geol.*, **206**, 289–318.
- Algeo, T.J. and Tribovillard, N.** (2009) Environmental analysis of paleoceanographic systems based on molybdenum-uranium covariation. *Chem. Geol.*, **268**, 211–225.
- Amblés, A., Halim, M., Jacquesy, J.C., Vitorovic, D. and Ziyad, M.** (1994) Characterization of kerogen from Timahdit shale (Y-layer) based on multistage alkaline permanganate degradation. *Fuel*, **73**, 17–24.
- Anderson, R.K., Scalan, R.S., Parker, R.L. and Behrens, E.W.** (1983) Seep oil and gas in Gulf of Mexico slope sediments. *Science*, **222**, 619–622.
- Anderson, S.J., Taylor, A.C. and Atkinson, R.J.A.** (1994) Anaerobic metabolism during anoxia in the burrowing shrimp *Calocaris macandreaea* Bell (Crustacea: Thalassinidea). *Comp. Biochem. Phys. A*, **108**, 515–522.
- Arthur, M.A. and Sageman, B.** (1994) Marine black shales, depositional mechanisms and environments of ancient deposits. *Annu. Rev. Earth Pl. Sc.*, **22**, 499–551.
- Arthur, M.A., Dean, W.E. and Schlanger, S.O.** (1985) Variations in the global carbon cycle during the Cretaceous related to climate, volcanism, and changes in atmospheric CO_2 . In: *The Carbon Cycle and Atmospheric CO_2 : Natural Variations Archean to Present* (Eds E.T. Sundquist and W.S. Broecker), *Geophys. Monogr. Ser.*, **32**, 504–529. AGU, Washington, DC.
- Astin, T.R. and Scotchman, T.C.** (1988) The diagenetic history of some septarian concretions from the Kimmeridge clay, England. *Sedimentology*, **35**, 349–368.
- Ayoub-Hannaa, W., Fürsich, F.T. and El Qot, G.M.** (2014) Cenomanian-Turonian bivalves from eastern Sinai, Egypt. *Palaeontogr. Abt. A*, **301**, 63–168.
- Barron, E.J.** (1983) A warm, equable Cretaceous: the nature of the problem. *Earth Sci. Rev.*, **19**, 305–338.
- Baudin, F.** (1995) Depositional controls on Mesozoic source rocks in the Tethys. In: *Paleogeography, Paleoclimate, and Source Rock* (Ed. A.Y. Huc), *AAPG Stud. Geol.*, **40**, 191–211.

- Beauchamp, B.** and **Savard, M.** (1992) Cretaceous chemosynthetic carbonate mounds in the Canadian Arctic. *Palaeos*, **7**, 434–450.
- Birgel, D., Peckmann, J., Klautzsch, S., Thiel, V.** and **Reitner, J.** (2006) Anaerobic and aerobic oxidation of methane at late Cretaceous seeps in the Western Interior Seaway, USA. *Geomicrobiol J.*, **23**, 565–577.
- Birgel, D., Elvert, M., Han, X.** and **Peckmann, J.** (2008a) ^{13}C -depleted biphytanic acids as tracers of past anaerobic oxidation of methane. *Org. Geochem.*, **39**, 152–156.
- Birgel, D., Himmler, T., Freiwald, A.** and **Peckmann, J.** (2008b) A new constraint on the antiquity of anaerobic oxidation of methane: Late Pennsylvanian seep limestones from southern Namibia. *Geology*, **36**, 543–546.
- Bohrmann, G., Abelman, A., Gersonde, R., Hubberten, H.** and **Kuhn, G.** (1994) Pure siliceous ooze, a diagenetic environment for early chert formation. *Geology*, **22**, 207–210.
- Bonarelli, G.** (1891) *Il territorio di Gubbio*. Notizie Geologiche: Tipografia Economica, Roma, 38 pp.
- Bramlette, M.N.** and **Sullivan, F.R.** (1961) Coccolithophorids and related nannoplankton of the early Tertiary in California. *Micropaleontology*, **7**, 129–174.
- Bromley, R.G.** (1996) *Trace Fossils: Biology, Taphonomy and Applications*, 2nd edn. Chapman and Hall, London, 361 pp.
- Brumsack, H.J.** (1980) Geochemistry of Cretaceous black shales from the Atlantic Ocean (DSDP Legs 11, 14, 36, and 41). *Chem. Geol.*, **31**, 1–25.
- Brumsack, H.J.** (2006) The trace metal content of recent organic carbon-rich sediments: implications for Cretaceous black shale formation. *Palaeogeogr. Palaeoclimatol. Palaeoecol.*, **232**, 344–361.
- Busson, G., Dhondt, A., Amédéo, F., Néraudeau, D.** and **Cornée, A.** (1999) La grande transgression du Cénomanién supérieur-Turonien inférieur sur la Hamada de Tinrhert (Sahara algérien): datations biostratigraphiques, environnement de dépôt et comparaison d'un témoin épïcratonique avec les séries contemporaines à matière organique du Maghreb. *Cretaceous Res.*, **20**, 29–46.
- Calvert, S.E.** and **Pedersen, T.F.** (1993) Geochemistry of recent oxic and anoxic marine sediments – implications for the geological record. *Mar. Geol.*, **113**, 67–88.
- Campbell, K.A.** (2006) Hydrocarbon seep and hydrothermal vent paleoenvironments and paleontology: past developments and future directions. *Palaeogeogr. Palaeoclimatol. Palaeoecol.*, **232**, 362–407.
- Campbell, K.A.** and **Bottjer, D.J.** (1995) Brachiopods and chemosymbiotic bivalves in Phanerozoic hydrothermal vent and cold seep environments. *Geology*, **23**, 321–324.
- Campbell, K.A., Farmer, J.D.** and **Des Marais, D.** (2002) Ancient hydrocarbon seeps from the Mesozoic convergent margin of California: carbonate geochemistry, fluids and paleoenvironments. *Geofluids*, **2**, 63–94.
- Carson, B.** and **Screaton, E.J.** (1998) Fluid flow in accretionary prisms: evidence for focused, time-variable discharge. *Rev. Geophys.*, **36**, 329–351.
- Coleman, M.L.** (1993) Microbial processes: controls on the shape and composition of carbonate concretions. *Mar. Geol.*, **113**, 127–140.
- Coleman, M.L.** and **Raiswell, R.** (1995) Source of carbonate and origin of zonation in pyritiferous carbonate concretions: evaluation of a dynamic model. *Am. J. Sci.*, **295**, 282–308.
- Collignon, M.** (1966) Les céphalopodes crétacés du bassin côtier de Tarfaya. *Service Geol. Maroc, Notes et Mem.*, **175**, 1–35.
- Conti, S., Fontana, D., Gubertini, A., Sighinolfi, G., Tateo, F., Fioroni, C.** and **Fregni, P.** (2004) A multidisciplinary study of middle Miocene seep-carbonates from the northern Apennine foredeep (Italy). *Sed. Geol.*, **169**, 1–19.
- Crusius, J., Calvert, S., Pedersen, T.** and **Sage, D.** (1996) Rhenium and molybdenum enrichments in sediments as indicators of oxic, suboxic and sulfidic conditions of deposition. *Earth Planet. Sci. Lett.*, **145**, 65–78.
- Dando, P.R., Southward, A.J.** and **Southward, E.C.** (1986) Chemoautotrophic symbionts in the gills of the bivalve mollusc *Lucinoma borealis* and the sediment chemistry of its habitat. *P. R. Soc. London B. Biol.*, **227**, 227–247.
- De Boever, E., Birgel, D., Thiel, V., Muchez, P., Peckmann, J., Dimitrov, L.** and **Swennen, R.** (2009) The formation of giant tubular concretions triggered by anaerobic oxidation of methane as revealed by archaeal molecular fossils (Lower Eocene, Varna, Bulgaria). *Palaeogeogr. Palaeoclimatol. Palaeoecol.*, **280**, 23–36.
- DeMaster, D.J.** (2002) The accumulation and cycling of biogenic silica in the Southern Ocean: revisiting the marine silica budget. *Deep-Sea Res. Pt. II*, **49**, 3155–3167.
- Dickson, J.A.D.** (1966) Carbonate identification and genesis as revealed by staining. *J. Sed. Petrol.*, **36**, 491–505.
- El Albani, A., Caron, M., Deconinck, J.-F., Robazynski, F., Amédéo, F., Daoudi, L., Ezaidi, A., Terrab, S.** and **Thurrow, J.** (1997) Origin of nodules in Lower Turonian organic-rich sediments in Tarfaya Basin (Southwest Morocco). *CR Acad. Sci. Ser. IIA Earth Planet. Sci.*, **324**, 9–16.
- El Albani, A., Kuhnt, W., Luderer, F., Herbin, J.P.** and **Caron, M.** (1999a) Palaeoenvironmental evolution of the Late Cretaceous sequence in the Tarfaya Basin (Southwest of Morocco). In: *The Oil and Gas Habitats of the South Atlantic* (Eds N.R. Cameron, R.H. Bate and V.S. Clure), *Geol. Soc. London. Spec. Publ.*, **153**, 223–240.
- El Albani, A., Vachard, D., Kuhnt, W.** and **Chellai, H.** (1999b) Signature of hydrodynamic activity caused by rapid sea level changes in pelagic organic-rich sediments, Tarfaya Basin (southern Morocco). *CR Acad. Sci. Ser. IIA Earth Planet. Sci.*, **329**, 397–404.
- El Albani, A., Vachard, D., Kuhnt, W.** and **Thurrow, J.** (2001) The role of diagenetic carbonate concretions in the

- preservation of the original sedimentary record. *Sedimentology*, **48**, 875–886.
- El Qot, G.M.** (2006) Late Cretaceous macrofossils from Sinai, Egypt. *Beringeria*, **36**, 3–163.
- Erba, E., Castradori, D., Guasti, G. and Ripepe, M.** (1992) Calcareous nannofossils and Milankovitch cycles: the example of the Albian Gault Clay Formation (Southern England). *Palaeogeogr. Palaeoclimatol. Palaeoecol.*, **93**, 47–69.
- Eshet, Y. and Almogi-Labin, A.** (1996) Calcareous nannofossils as paleoproductivity indicators in Upper Cretaceous organic-rich sequences in Israel. *Mar. Micropaleontol.*, **29**, 37–61.
- Feng, D., Birgel, D., Peckmann, J., Roberts, H.H., Joye, S.B., Sassen, R., Liu, X.-L., Hinrichs, K.-U. and Chen, D.** (2014) Time integrated variation of sources of fluids and seepage dynamics archived in authigenic carbonates from Gulf of Mexico Gas Hydrate Seafloor Observatory. *Chem. Geol.*, **385**, 129–139.
- Formolo, M.J., Lyons, T.W., Zhang, C., Kelley, C., Sassen, R., Horita, J. and Cole, D.R.** (2004) Quantifying carbon sources in the formation of authigenic carbonates at gas hydrate sites in the Gulf of Mexico. *Chem. Geol.*, **205**, 253–264.
- Forster, S. and Graf, G.** (1992) Continuously measured changes in redox potential influenced by oxygen penetrating from burrows of *Callianassa subterranea*. *Hydrobiologia*, **235**, 527–532.
- Forster, A., Schouten, S., Moriya, K., Wilson, P.A. and Sinninghe Damsté, J.S.** (2007) Tropical warming and intermittent cooling during the Cenomanian/Turonian oceanic anoxic event 2: sea surface temperature records from the equatorial Atlantic. *Paleoceanography*, **22**, PA1219. doi:10.1029/2006PA001349.
- Gale, A.S., Smith, A.B., Monks, N.E.A., Young, J.A., Howard, A., Wray, D.S. and Huggett, J.M.** (2000) Marine biodiversity through the Late Cenomanian–Early Turonian: paleoceanographic controls and sequence stratigraphic biases. *J. Geol. Soc. London*, **157**, 745–757.
- Gebhardt, H., Kuhnt, W. and Holbourn, A.** (2004) Foraminiferal response to sea level change, organic flux and oxygen deficiency in the Cenomanian of the Tarfaya Basin, southern Morocco. *Mar. Micropaleontol.*, **53**, 133–157.
- Gertsch, B., Adatte, T., Keller, G., Tantawy, A.A.A., Berner, Z., Mort, H.P. and Fleitmann, D.** (2010) Middle and late Cenomanian oceanic anoxic events in shallow and deeper shelf environments of western Morocco. *Sedimentology*, **57**, 1430–1462.
- Goedert, J.L., Peckmann, J. and Reitner, J.** (2000) Worm tubes in an allochthonous cold-seep carbonate from lower Oligocene rocks of western Washington. *J. Paleontol.*, **74**, 992–999.
- Greiner, J., Bohrmann, G. and Suess, E.** (2001) Gas hydrate-associated carbonates and methane-venting at Hydrate Ridge: classification, distribution, and origin of authigenic lithologies. *Geoph. Monog.*, **124**, 99–113.
- Guido, A., Heindel, K., Birgel, D., Rosso, A., Mastandrea, A., Sanfilippo, R., Russo, F. and Peckmann, J.** (2013) Pendant bioconstructions cemented by microbial carbonate in submerged marine caves (Holocene, SE Sicily). *Palaeogeogr. Palaeoclimatol. Palaeoecol.*, **388**, 166–180.
- Haas, A., Peckmann, J., Elvert, M., Sahling, H. and Bohrmann, G.** (2010) Patterns of carbonate authigenesis at the Kouilou pockmarks on the Congo deep-sea fan. *Mar. Geol.*, **268**, 129–136.
- Hagemann, A., Leefmann, T., Peckmann, J., Hoffmann, V.-E. and Thiel, V.** (2013) Biomarkers from individual carbonate phases of an Oligocene cold-seep deposit, Washington State, USA. *Lethaia*, **46**, 7–18.
- Hallam, A. and Bradshaw, A.** (1977) Bituminous shales and oolitic ironstones as indicators of transgressions and regressions. *J. Geol. Soc. London*, **36**, 57–64.
- Handoh, I.C., Bigg, G.R., Jones, E.J.W. and Inoue, M.** (1999) An ocean modeling study of the Cenomanian Atlantic: equatorial paleoupwelling, organic-rich sediments and the consequences for a connection between the proto-North and South Atlantic. *Geophys. Res. Lett.*, **26**, 223–226.
- Haq, B.U.** (2014) Cretaceous eustasy revisited. *Global Planet. Change*, **113**, 44–58.
- Hardenbol, J., Thierry, J., Farley, M.B., Jacquin, T., De Graciansky, P.C. and Vail, P.R.** (1998) Mesozoic and Cenozoic sequence chronostratigraphic framework of European Basins. *SEPM Spec. Publ.*, **60**, 3–13.
- Hattner, J.G., Wind, F.H. and Wise, S.W.** (1980) The Santonian–Campanian boundary. Comparison of nearshore-offshore calcareous nannofossil assemblages. *Cah. Micropaleontol.*, **3**, 9–26.
- Hay, W.W.** (1961) Note on the preparation of samples for discoasterids. *J. Paleontol.*, **35**, 873.
- Hay, W.W.** (1965) Calcareous nannofossils. In: *Handbook of Paleontological Techniques* (Eds. B. Kummel and D. Raup), pp. 3–7. Freeman, San Francisco, CA.
- Heany, P.J.** (1993) A proposed mechanism for the growth of chalcedony. *Contrib. Mineral. Petrol.*, **115**, 66–74.
- Heinrichs, H., Brumsack, H.-J., Loftfield, N. and König, N.** (1986) Verbessertes Druckaufschlußsystem für biologische und anorganische Materialien. *Z. Pflanzenernähr. Bodenk.*, **149**, 350–353.
- Helz, G.R., Miller, C.V., Charnick, J.M., Mosselmans, J.F.W., Patrick, R.A.D., Garner, C.D. and Vaughan, D.J.** (1996) Mechanism of molybdenum removal from the sea and its concentration in black shales: EXAFS evidence. *Geochim. Cosmochim. Acta*, **60**, 3631–3642.
- Herbin, J.P., Montadert, L., Mueller, C., Gomez, R., Thurow, J. and Wiedmann, J.** (1986) Organic-rich sedimentation at the Cenomanian–Turonian Boundary in oceanic and coastal basins in the North Atlantic and Tethys. In: *North Atlantic*

- Palaeoceanography* (Eds C. Summerhayes and N.J. Shackleton), *Geol. Soc. London*, **21**, 389–422.
- Herrle, J.O.** (2003) Reconstructing nutricline dynamics of mid-Cretaceous oceans: evidence from calcareous nannofossils from the Niveau Paquier black shale (SE France). *Mar. Micropalaeontol.*, **47**, 307–321.
- Hetzel, A., Böttcher, M.E., Wortmann, U.G. and Brumsack, H.-J.** (2009) Paleo-redox conditions during OAE 2 reflected in Demarara Rise sediment geochemistry (ODP Leg 207). *Palaeogeogr. Palaeoclimatol. Palaeoecol.*, **273**, 302–328.
- Himmler, T., Freiwald, A., Stollhofen, H. and Peckmann, J.** (2008) Late Carboniferous hydrocarbon-seep carbonates from the glaciomarine Dwyka Group, southern Namibia. *Palaeogeogr. Palaeoclimatol. Palaeoecol.*, **257**, 185–197.
- Holbourn, A., Kuhnt, W., El Albani, A., Pletsch, T., Luderer, F. and Wagner, T.** (1999) Upper Cretaceous palaeoenvironments and benthonic foraminiferal assemblages of potential source rocks from the western African margin, Central Atlantic. In: *The Oil and Gas Habitats of the South Atlantic* (Eds N.R. Cameron, R.H. Bate and V.S. Clure), *Geol. Soc. London. Spec. Publ.*, **153**, 195–222.
- Hudson, J.D.** (1978) Concretions, isotopes and the diagenetic history of the Oxyford Clay (Jurassic) of central England. *Sedimentology*, **25**, 339–370.
- Hudson, J.D. and Friedman, I.** (1974) Carbon and oxygen isotopes in concretions: relationship to pore water changes during diagenesis. In: *Proceedings of the International Symposium on Water-Rock Interaction* (Eds. J. Cadetm and T. Paces), pp. 331–339. Geological Survey, Prague.
- Ingall, E.D., Bustin, R.M. and Van Cappellen, P.** (1993) Influence of water column anoxia on the burial and preservation of carbon and phosphorus in marine shales. *Geochim. Cosmochim. Acta*, **57**, 303–316.
- Jenkyns, H.C.** (2003) Evidence for rapid climate change in the Mesozoic-Palaeogene greenhouse world. *Philos. T. R. Soc. London*, **361**, 1885–1916.
- Jenkyns, H.C.** (2010) Geochemistry of oceanic anoxic events. *Geochim. Geophys. Geosys.*, **11**, 1–30.
- Jenkyns, H.C., Matthews, A., Tsikos, H. and Erel, Y.** (2007) Nitrate reduction, sulfate reduction, and sedimentary iron isotope evolution during the Cenomanian – Turonian oceanic anoxic event. *Palaeoceanography*, **22**, 1–17.
- Jones, C.E. and Jenkyns, H.C.** (2001) Seawater strontium isotopes, oceanic anoxic events, and seafloor hydrothermal activity in the Jurassic and Cretaceous. *Am. J. Sci.*, **301**, 112–149.
- Judd, A.J. and Hovland, M.** (2007) *Submarine Fluid Flow, the Impact on Geology, Biology, and the Marine Environment*. Cambridge University Press, Cambridge.
- Kaiho, K.** (1994) Benthic foraminiferal dissolved-oxygen index and dissolved-oxygen levels in the modern ocean. *Geology*, **22**, 719–722.
- Kasten, S., Zabel, M., Heuer, V. and Hensen, C.** (2003) Processes and signals of nonsteady-state diagenesis in deep-sea sediments and their pore waters. *The South Atlantic in the Late Quaternary*, pp. 431–459. Springer, Berlin, Heidelberg.
- Kauffman, E.G., Arthur, M.A., Howe, B. and Scholle, P.A.** (1996) Widespread venting of methane-rich fluids in Late Cretaceous (Campanian) submarine springs (Tepee Buttes), Western Interior seaway, U.S.A. *Geology*, **24**, 799–802.
- Keene, J.B.** (1975) Cherts and porcellanites from the North Pacific. *Initial Rep. Deep Sea.*, **32**, 429–507.
- Kerr, A.C.** (1998) Oceanic plateau formation: a cause of mass extinction and black shale deposition around the Cenomanian-Turonian boundary? *J. Geol. Soc. London*, **155**, 619–626.
- Kiel, S.** (2010) On the potential generality of depth-related ecologic structure in cold-seep communities: evidence from Cenozoic and Mesozoic examples. *Palaeogeogr. Palaeoclimatol. Palaeoecol.*, **295**, 245–257.
- Kiel, S.** (2013) Lucinid bivalves from ancient methane seeps. *J. Malacol. Soc. London*, **79**, 346–363.
- Kiel, S. and Peckmann, J.** (2007) Chemosymbiotic bivalves and stable carbon isotopes indicate hydrocarbon seepage at four unusual Cenozoic fossil localities. *Lethaia*, **40**, 345–357.
- Kiel, S., Wiese, F. and Titus, A.L.** (2012) Shallow-water methane-seep faunas in the Cenomanian Western Interior Seaway: no evidence for onshore-offshore adaptations to deep-sea vents. *Geology*, **40**, 839–842.
- Kiel, S., Birgel, D., Campbell, K.A., Crampton, J.S., Schiøler, P. and Peckmann, J.** (2013) Cretaceous methane-seep deposits from New Zealand and their fauna. *Palaeogeogr. Palaeoclimatol. Palaeoecol.*, **390**, 17–34.
- Knauth, P.L.** (1994) Petrogenesis of chert. In: *Reviews in Mineralogy, vol. 29: Silica – Physical Behavior, Geochemistry and Materials Applications* (Eds. P.W. Heany, C.T. Prewitt and G.V. Gibbs), pp. 233–258. Mineralogical Society of America, Washington, DC.
- Kolonc, S., Sinninghe Damsté, J.S., Böttcher, M.E., Kuypers, M.M.M., Kuhnt, W., Beckmann, B., Scheeder, G. and Wagner, T.** (2002) Geochemical characterization of Cenomanian/Turonian black shales from the Tarfaya Basin (SW Morocco): relationships between paleoenvironmental conditions and early sulfurization of sedimentary organic matter. *J. Petrol. Geol.*, **25**, 325–350.
- Kolonc, S., Wagner, T., Forster, A., Sinninghe Damsté, J.S., Walsworth-Bell, B., Erba, E., Turgeon, S., Brumsack, H.J., Chellai, E.H., Tsikos, H., Kuhnt, W. and Kuypers, M.M.M.** (2005) Black shale deposition on the northwest African shelf during the Cenomanian-Turonian oceanic anoxic event: climate coupling and global organic carbon burial. *Palaeoceanography*, **20**, 1–18.
- Könneke, M., Lipp, J.S. and Hinrichs, K.-U.** (2012) Carbon isotope fractionation by the marine ammonia-oxidizing archaeon *Nitrosopumilus maritimus*. *Org. Geochem.*, **48**, 12–24.
- Kuechler, R.R., Birgel, D., Kiel, S., Freiwald, A., Goedert, J.L., Thiel, V. and Peckmann, J.** (2012) Miocene methane-

- derived carbonates from southwestern Washington (USA) and a model for silicification at seeps. *Lethaia*, **45**, 259–273.
- Kuhnt, W. and Wiedmann, J.** (1995) Cenomanian–Turonian source rocks: paleobiogeographic and paleoenvironmental aspects. In: *Paleogeography, Paleoclimate and Source Rocks* (Ed. A.Y. Huc), *Stud. Geol.*, **40**, 213–232. AAPG, Tulsa, OK.
- Kuhnt, W., Herbin, J.P., Thurow, J. and Wiedmann, J.** (1990) Distribution of Cenomanian–Turonian organic facies in the western Mediterranean and along the adjacent Atlantic margin. In: *Deposition of Organic Facies* (Ed. A.Y. Huc), *AAPG Stud. Geol.*, **30**, 133–160.
- Kuhnt, W., El Chellai, H., Holbourn, A., Luderer, F., Thurow, J., Wagner, T., El Albani, A., Beckmann, B., Herbin, J.P., Kawamura, H., Kolonic, S., Nederbragt, S., Street, C. and Ravilious, K.** (2001) Morocco basin's sedimentary record may provide correlations for Cretaceous paleoceanographic events worldwide. *EOS Trans. Am. Geophys. Union*, **82**, 361–364.
- Kuhnt, W., Luderer, F., Nederbragt, A., Thurow, J. and Wagner, T.** (2005) Millennial resolution record of the Late Cenomanian Oceanic Anoxic Event (OAE2) in the Tarfaya Basin (Morocco). *Int. J. Earth Sci.*, **94**, 147–159.
- Kuhnt, W., Holbourn, A., Gale, A., Chellai, E.H. and Kennedy, W.J.** (2009) Cenomanian sequence stratigraphy and sea-level fluctuations in the Tarfaya Basin (SW Morocco). *Geol. Soc. Am. Bull.*, **121**, 1695–1710.
- Kuypers, M.M.M., Pancost, R.D., Nijenhuis, I.A. and Sinninghe Damsté, J.S.** (2002) Enhanced productivity led to increased organic carbon burial in the euxinic North Atlantic basin during the late Cenomanian oceanic anoxic event. *Paleoceanography*, **17**, 1–13.
- Lancelot, Y.** (1973) Chert and silica diagenesis in sediments from the central Pacific. *Initial Rep. Deep Sea*, **32**, 429–507.
- Larson, R.L.** (1991) Latest pulse of Earth; evidence for a mid-Cretaceous super-plume. *Geology*, **19**, 547–550.
- Larson, R.L. and Erba, E.** (1999) Onset of the Mid-Cretaceous greenhouse in the Barremian–Aptian: igneous events and the biological, sedimentary, and geochemical responses. *Paleoceanography*, **14**, 663–678.
- Layeb, M., Fadhel, M.B. and Youssef, M.B.** (2012) Thrombolitic and coral buildups in the Upper Albian of the Fahdene basin (North Tunisia): stratigraphy, sedimentology and genesis. *Bull. Soc. Géol. France*, **183**, 217–231.
- Layeb, M., Fadhel, M.B., Layeb-Tounsi, Y. and Youssef, M.B.** (2014) First microbialites associated to organic-rich facies of the Oceanic Anoxic Event 2 (Northern Tunisia, Cenomanian–Turonian transition). *Arab. J. Geosc.*, **7**, 3349–3363.
- Leine, L.** (1986) Geology of the Tarfaya oil shale deposit, Morocco. *Geol. Mijnbouw*, **65**, 57–74.
- Liang, H., Chen, X., Wang, C., Zhao, D. and Weissert, H.** (2016) Methane-derived authigenic carbonates of mid-Cretaceous age in southern Tibet: types of carbonate concretions, carbon sources, and formation processes. *J. Asian Earth Sci.*, **115**, 153–169.
- Little, C.T.S., Birgel, D., Boyce, A.J., Crame, A.J., Francis, J.E., Kiel, S., Peckmann, J., Pirrie, D., Rollinson, G.K. and Witts, J.D.** (2015) Late Cretaceous (Maastrichtian) shallow water hydrocarbon seeps from Snow Hill and Seymour Islands, James Ross Basin, Antarctica. *Palaeogeogr. Palaeoclimatol. Palaeoecol.*, **418**, 213–228.
- Liu, X.-L., Birgel, D., Elling, F.J., Sutton, P.A., Lipp, J.S., Zhu, R., Zhang, C., Könneke, M., Peckmann, J., Rowland, S., Summons, R.E. and Hinrichs, K.-U.** (2016) From ether to acid: a plausible degradation pathway of glycerol dialkyl glycerol tetraethers. *Geochim. Cosmochim. Acta*, **183**, 138–152.
- Lüning, S., Marzouk, A.M. and Kuss, J.** (1998) Latest Maastrichtian high frequency litho- and ecocycles from the hemipelagic of Eastern Sinai, Egypt. *J. Afr. Earth Sci.*, **27**, 373–395.
- Lüning, S., Kolonic, S., Belhadj, E.M., Belhadj, Z., Cota, L., Baric, G. and Wagner, T.** (2004) Integrated depositional model for the Cenomanian–Turonian organic-rich strata in North Africa. *Earth Sci. Rev.*, **64**, 51–117.
- Marshall, J.D. and Pirrie, D.** (2013) Carbonate concretions – explained. *Geol. Today*, **29**, 53–62.
- Marzouk, A.M. and Lüning, S.** (2005) Calcareous nannofossil biostratigraphy and distribution patterns in the Cenomanian–Turonian of North Africa. *Grmena*, **1**, 107–122.
- Masclé, J., Lohmann, G.P., Clift, P.D. and Party, S.S.** (1997) Development of a passive transform margin: Cote d'Ivoire–Ghana transform margin — ODP Leg 159 preliminary results. *Geo-Mar. Lett.*, **17**, 4–11.
- Mattioli, E.** (1997) Nannoplankton productivity and diagenesis in the rhythmically bedded Toarcian–Aalenian Fiuminata sequence (Umbria–Marche Apennine, Central Italy). *Palaeogeogr. Palaeoclimatol. Palaeoecol.*, **130**, 113–134.
- McAnena, A., Floegel, S., Hofmann, P., Herrle, J.O., Griesand, A., Pross, J., Talbot, H.M., Rethemeyer, L., Wallmann, K. and Wagner, T.** (2013) Atlantic opening, million-year cooling and coupled marine biotic crises in the Cretaceous. *Nat. Geosci.*, **6**, 558–561.
- Metz, C.L.** (2010) Tectonic controls on the genesis and distribution of Late Cretaceous Western Interior Basin hydrocarbon-seep mounds (Tepee Buttes) of North America. *J. Geol.*, **118**, 201–213.
- Meyer, K.M. and Kump, L.R.** (2008) Oceanic euxinia in Earth history: causes and consequences. *Ann. Rev. Earth Planet. Sci.*, **36**, 251–288.
- Morford, J.L. and Emerson, S.R.** (1999) The geochemistry of redox sensitive trace metals in sediments. *Geochim. Cosmochim. Acta*, **63**, 1735–1750.
- Morford, J.L., Emerson, S.R., Breckel, E.J. and Kim, S.H.** (2005) Diagenesis of oxyanions (V, U, R, and Mo) in pore

- waters and sediments from a continental margin. *Geochim. Cosmochim. Acta*, **69**, 5021–5032.
- Mort, H.P., Adatte, T., Keller, G., Bartels, D., Föllmi, K.B., Steinmann, P., Berner, Z. and Chellai, E.H.** (2008) Organic carbon deposition and phosphorus accumulation during Oceanic Anoxic Event 2 in Tarfaya. *Morocco. Cretaceous Res.*, **29**, 1008–1023.
- Mozley, P.S. and Davis, J.M.** (2005) Internal structure and mode of growth of elongate calcite concretions: evidence for small-scale, microbially induced, chemical heterogeneity in groundwater. *Geol. Sci. Am. Bull.*, **117**, 1400–1412.
- Naehr, T.H., Birgel, D., Bohrmann, G., MacDonald, I.R. and Kasten, S.** (2009) Biogeochemical controls on authigenic carbonate formation at the Chaopopote “asphalt volcano”, Bay of Campeche. *Chem. Geol.*, **266**, 390–402.
- Natalicchio, M., Birgel, D., Dela Pierre, F., Martire, L., Clari, P., Spötl, C. and Peckmann, J.** (2012) Polyphasic carbonate precipitation in the shallow subsurface: insights from microbially-formed authigenic carbonate beds in upper Miocene sediments of the Tertiary Piedmont Basin (NW Italy). *Palaeogeogr. Palaeoclimatol. Palaeoecol.*, **329–330**, 158–172.
- Nederbragt, A.J. and Fiorentino, A.** (1999) Stratigraphy and palaeoceanography of the Cenomanian-Turonian Boundary Event in Oued Mellegue, north–western Tunisia. *Cretaceous Res.*, **20**, 47–62.
- Nöthen, K. and Kasten, S.** (2011) Reconstructing changes in seep activity by means of pore water and solid phase Sr/Ca and Mg/Ca ratios in pockmark sediments of the Northern Congo Fan. *Mar. Geol.*, **287**, 1–13.
- Owens, J.D., Gill, B.C., Jenkyns, H.C., Bates, S.M., Severmann, S., Kuypers, M.M.M., Woodfine, R.G. and Lyons, T.W.** (2013) Sulfur isotopes track the global extent and dynamics of euxinia during Cretaceous Oceanic Anoxic Event 2. *Proc. Natl Acad. Sci. USA*, **110**, 18407–18412.
- Pearson, A., Hurley, S.J., Walter, S.R.S., Kusch, S., Lichtin, S. and Zhang, Y.G.** (2016) Stable carbon isotope ratios of intact GDGTs indicate heterogenous sources to marine sediments. *Geochim. Cosmochim. Acta*, **181**, 18–35.
- Peckmann, J. and Thiel, V.** (2004) Carbon cycling at ancient methane seeps. *Chem. Geol.*, **205**, 443–467.
- Peckmann, J., Thiel, V., Michaelis, W., Clari, P., Gaillard, P., Martire, L. and Reitner, J.** (1999) Cold seep deposits of Beauvoisin (Oxfordian; southeastern France) and Marmorito (Miocene; northern Italy): microbially induced authigenic carbonates. *Int. J. Earth Sci.*, **88**, 60–75.
- Peckmann, J., Reimer, A., Luth, U., Luth, C., Hansen, B.T., Heinicke, C., Hoefs, J. and Reitner, J.** (2001) Methane derived carbonates and authigenic pyrite from the northwestern Black Sea. *Mar. Geol.*, **177**, 129–150.
- Peckmann, J., Goedert, J.L., Thiel, V., Michaelis, W. and Reitner, J.** (2002) A comprehensive approach to the study of methane–seep deposits from the Lincoln Creek Formation, western Washington State USA. *Sedimentology*, **49**, 855–873.
- Peckmann, J., Goedert, J.L., Heinrichs, T., Hoefs, J. and Reitner, J.** (2003) The late Eocene ‘Whiskey Creek’ methane-seep deposit (western Washington State). Part II: petrology, stable isotopes, and biogeochemistry. *Facies*, **48**, 241–254.
- Peckmann, J., Senowbari-Daryan, B., Birgel, D. and Goedert, J.L.** (2007) The crustacean ichnofossil *Palaxius* associated with callianassid body fossils in an Eocene methane-seep limestone, Humptulips Formation, Olympic Peninsula, Washington. *Lethaia*, **40**, 273–280.
- Peckmann, J., Birgel, D. and Kiel, S.** (2009) Molecular fossils reveal fluid composition and flow intensity at a Cretaceous seep. *Geology*, **37**, 847–850.
- Peckmann, J., Kiel, S., Sandy, M.R., Taylor, D.G. and Goedert, J.L.** (2011) Mass occurrences of the brachiopod *Halorella* in Late Triassic methane-seep deposits, eastern Oregon. *J. Geol.*, **119**, 207–220.
- Poulton, S.W., Henkel, S., März, C., Urquhart, H., Floegel, S., Kasten, S., Sinninghe Damsté, J. and Wagner, T.** (2015) A continental-weathering control on orbitally driven redox-nutrient cycling during Cretaceous Oceanic Anoxic Event 2. *Geology*, **43**, 963–966.
- Raiswell, R. and Fischer, Q.J.** (2004) Rates of carbonate cementation associated with sulphate reduction in DSDP/ODP sediments: implications for the formation of concretions. *Chem. Geol.*, **211**, 71–85.
- Raiswell, R. and Fisher, Q.J.** (2000) Mudrock-hosted carbonate concretions: a review of growth mechanisms and their influence on chemical and isotopic composition. *J. Geol. Soc. London*, **157**, 239–251.
- Reitz, A., Hensen, C., Kasten, S., Funk, J.A. and De Lange, G.J.** (2004) A combined geochemical and rock-magnetic investigation of a redox horizon at the last glacial/interglacial transition. *Phys. Chem. Earth*, **29**, 921–931.
- Ritger, S., Carson, B. and Suess, E.** (1987) Methane derived authigenic carbonates formed by subduction-induced pore-water expulsion along the Oregon/Washington margin. *Geol. Soc. Am. Bull.*, **98**, 147–156.
- Roberts, H.H. and Aharon, P.** (1994) Hydrocarbon-derived carbonate buildups of the northern Gulf of Mexico continental slope: a review of submersible investigations. *Geo-Mar. Lett.*, **14**, 135–148.
- Roberts, H.H., Aharon, P. and Walsh, M.M.** (1993) Cold-seep carbonates of the Louisiana continental slope-to-basin floor. In: *Carbonate Microfabrics* (Eds R. Rezak and D.L. Lavoie), pp. 95–104. Springer, Berlin, Heidelberg, New York.
- Rosenthal, Y., Lam, P., Boyle, E.A. and Thomson, J.** (1995) Authigenic cadmium enrichments in suboxic sediments: precipitation and postdepositional mobility. *Earth Planet. Sci. Lett.*, **132**, 99–111.

- Roth, P.H.** (1981) Mid-Cretaceous calcareous nannoplankton from the central Pacific: implication for paleoceanography. *Initial Rep. Deep Sea*, **62**, 471–489.
- Roth, P.H.** and **Krumbach, K.R.** (1986) Middle Cretaceous calcareous nannofossil biogeography and preservation in the Atlantic and Indian Oceans: implications for paleoceanography. *Mar. Micropaleontol.*, **10**, 235–266.
- Sachse, V.F., Littke, R., Jabour, H., Schumann, T. and Kluth, O.** (2012) Late Cretaceous (Late Turonian, Coniacian and Santonian) petroleum source rocks as part of an OAE, Tarfaya Basin, Morocco. *Mar. Petrol. Geol.*, **29**, 35–49.
- Sames, B., Wagreich, M., Wendler, J.E., Haq, B.U., Conrad, C.P., Dobrinescu-Melinte, M.C., Hu, X., Wendler, I., Wolfgring, E., Yilmaz, I.Ö. and Zorina, S.O.** (2016) Review: short-term sea-level changes in a greenhouse world – a view from the Cretaceous. *Palaeogeogr. Palaeoclimatol. Palaeoecol.*, **441**, 393–411.
- Sassen, R., Joye, S., Sweet, S.T., DeFreitas, D.A., Milkov, A.V. and MacDonald, I.R.** (1999) Thermogenic gas hydrates and hydrocarbon gases in complex chemosynthetic communities, Gulf of Mexico continental slope. *Org. Geochem.*, **30**, 485–497.
- Savard, M.M., Beauchamp, B. and Veizer, J.** (1996) Significance of aragonite cements around Cretaceous marine methane seeps. *J. Sed. Res.*, **66**, 430–438.
- Schlanger, S.O. and Jenkyns, H.C.** (1976) Cretaceous oceanic anoxic events: causes and consequences. *Geol. Mijnbouw*, **55**, 179–184.
- Schlanger, S.O., Arthur, M.A., Jenkyns, H.C. and Scholle, P.A.** (1987) The Cenomanian–Turonian oceanic anoxic event, I. Stratigraphy and distribution of organic carbon-rich beds and the marine $\delta^{13}\text{C}$ excursion. In: *Marine Petroleum Source Rocks* (Eds J. Brooks and A.J. Fleet), *Geol. Soc. Spec. Publ.*, **26**, 371–399.
- Schouten, S., Wakeham, S.T., Hopmans, E.C. and Sinninghe Damsté, J.S.** (2003) Biogeochemical evidence that thermophilic archaea mediate the anaerobic oxidation of methane. *Appl. Environ. Microb.*, **69**, 1680–1686.
- Schouten, S., Hopmans, E.C. and Sinninghe Damsté, J.S.** (2013) The organic geochemistry of glycerol dialkyl glycerol tetraether lipids: a review. *Org. Geochem.*, **54**, 19–61.
- Schwartz, H., Sample, J., Weberling, K.D., Minisini, D. and Moore, J.C.** (2003) An ancient linked fluid migration system: cold-seep deposits and sandstone intrusions in the Panoche Hills, California, USA. *Geo-Mar. Lett.*, **23**, 340–350.
- Schweigert, G., Seegis, D.B., Fels, A. and Leinfelder, R.R.** (1997) New internally structured decapod microcoprolites from Germany (Late Triassic/Early Miocene), Southern Spain (Early/Middle Jurassic) and Portugal (Late Jurassic): taxonomy, palaeoecology and evolutionary patterns. *Paläontol. Z.*, **71**, 51–69.
- Seilacher, A.** (2001) Concretion morphologies reflecting diagenetic and epigenetic pathways. *Sed. Geol.*, **143**, 41–57.
- Sellés-Martínez, J.** (1996) Concretion morphology, classification and genesis. *Earth Sci. Rev.*, **41**, 177–210.
- Snowbari-Daryan, B. and Kuss, J.** (1992) Anomuren-Koprolithen aus der Kreide von Ägypten. *Mitt. Geol.*, **73**, 129–157.
- Snowbari-Daryan, B., Weidlich, O. and Flügel, E.** (1992) Erster Nachweis von Favreinen (Crustaceen-Koprolithen) aus dem Perm: Oberperm, Oman-Berge. *Paläontol. Z.*, **6**, 187–196.
- Snowbari-Daryan, B., Gaillard, C. and Peckmann, J.** (2007) Crustacean microcoprolites from Jurassic (Oxfordian) hydrocarbon-seep deposits of Beauvoisin, southeastern France. *Facies*, **53**, 229–238.
- Shapiro, R. and Fricke, H.** (2002) Tepee Buttes: fossilized methane seep ecosystems. *Geol. Soc. Am. Field Guides*, **3**, 94–101.
- Sinninghe Damsté, J.S. and Köster, J.** (1998) A euxinic southern North Atlantic Ocean during the Cenomanian/Turonian oceanic anoxic event. *Earth Planet. Sci. Lett.*, **158**, 165–173.
- Smrzka, D., Kraemer, S.M., Zwicker, J., Birgel, D., Fischer, D., Kasten, S., Goedert, J.L. and Peckmann, J.** (2015) Constraining silica diagenesis in methane-seep deposits. *Palaeogeogr. Palaeoclimatol. Palaeoecol.*, **420**, 13–26.
- Smrzka, D., Zwicker, J., Klügel, A., Monien, P., Bach, W., Bohrmann, G. and Peckmann, J.** (2016) Establishing criteria to distinguish oil-seep from methane-seep carbonates. *Geology*, **44**, 667–670.
- Suess, E.** (2014) Marine cold seeps and their manifestations: geological control, biogeochemical criteria and environmental conditions. *Int. J. Earth Sci.*, **103**, 1889–1916.
- Suess, E. and Whiticar, M.J.** (1989) Methane-derived CO_2 in pore fluids expelled from the Orgeon subduction zone. *Palaeogeogr. Palaeoclimatol. Palaeoecol.*, **71**, 119–136.
- Teichert, B.M.A., Eisenhauer, A., Bohrmann, G., Haase-Schramm, A., Bock, B. and Linke, P.** (2003) U/Th Systematics and ages of authigenic carbonates from Hydrate Ridge, Cascadia Margin: recorders of fluid flow variations. *Geochim. Cosmochim. Acta*, **67**, 3845–3857.
- Thiel, V., Peckmann, J., Seifert, R., Wehrung, P., Reitner, J. and Michaelis, W.** (1999) Highly isotopically depleted isoprenoids: molecular markers for ancient methane venting. *Geochim. Cosmochim. Acta*, **63**, 3959–3966.
- Thierstein, H.R.** (1976) Mesozoic calcareous nannoplankton biostratigraphy of marine sediments. *Mar. Micropaleontol.*, **1**, 325–362.
- Tong, H., Wang, Q., Peckmann, J., Cao, Y., Chen, L., Zhou, W. and Chen, D.** (2016) Diagenetic alteration affecting $\delta^{18}\text{O}$, $\delta^{13}\text{C}$ and $^{87}\text{Sr}/^{86}\text{Sr}$ signatures of carbonates: a case study on Cretaceous seep deposits from Yarlung-Zangbo Suture Zone, Tibet, China. *Chem. Geol.*, **444**, 71–82.
- Tribouillard, N., Algeo, T.J., Lyons, T. and Riboulleau, A.** (2006) Trace metals as paleoredox and paleoproductivity proxies: an update. *Chem. Geol.*, **232**, 12–32.

- Von Rad, U., Riech, V. and Rösch, H.** (1977) Silica diagenesis in continental margin sediments off northwest Africa. *Initial Rep. Deep Sea*, **41**, 879–905.
- Wagner, T. and Pletsch, T.** (1999) Tectono-sedimentary controls on Cretaceous black shale deposition along the opening Equatorial Atlantic Gateway (ODP Leg 159). In: *Oil and Gas Habitats of the South Atlantic* (Eds N.R. Cameron, R.H. Bate and V.S. Clure), *Geol. Soc. London. Spec. Publ.*, **153**, 241–265.
- Wagner, T., Floegel, S. and Hofmann, P.** (2013) Marine black shale and Hadley Cell dynamics: a conceptual framework for the Cretaceous Atlantic Ocean. *Mar. Petrol. Geol.*, **43**, 222–238.
- Wedepohl, K.H.** (ed.) (1969) Composition and abundance of common igneous rocks. In: *Handbook of Geochemistry*, **1**, 227–249.
- Weissert, H.** (1981) The environment of deposition of black shales in the Early Cretaceous: an ongoing controversy. *SEPM Spec. Publ.*, **32**, 547–560.
- Weissert, H., McKenzie, J. and Hochuli, P.** (1979) Cyclic anoxic events in the Early Cretaceous Tethys Ocean. *Geology*, **7**, 147–151.
- Xu, W., Ruhl, M., Hesselbo, S.P., Riding, J.B. and Jenkyns, H.C.** (2016) Orbital pacing of the Early Jurassic carbon cycle, black shale formation and seabed methane seepage. *Sedimentology*, **64**, 127–149.
- Zwicker, J., Smrzka, D., Gier, S., Goedert, J.L. and Peckmann, J.** (2015) Mineralized conduits are part of the uppermost plumbing system of Oligocene methane-seep deposits, Washington State (USA). *Mar. Petrol. Geol.*, **66**, 616–630.